

(12) INTERNATIONAL APPLICATION PUBLISHED UNDER THE PATENT COOPERATION TREATY (PCT)

(19) World Intellectual Property Organization  
International Bureau



(43) International Publication Date  
7 June 2001 (07.06.2001)

PCT

(10) International Publication Number  
**WO 01/39873 A1**

- (51) International Patent Classification<sup>7</sup>: **B01F 3/12, C09K 3/00**
- (21) International Application Number: **PCT/US00/32961**
- (22) International Filing Date: 4 December 2000 (04.12.2000)
- (25) Filing Language: English
- (26) Publication Language: English
- (30) Priority Data:  
60/168,884 3 December 1999 (03.12.1999) US  
60/168,892 3 December 1999 (03.12.1999) US
- (71) Applicant (for all designated States except US): **THE PENNSYLVANIA STATE UNIVERSITY** [US/US]; 113 Technology Center, University Park, PA 16802-7000 (US).
- (72) Inventors; and
- (75) Inventors/Applicants (for US only): **NATAN, Michael, J.** [US/US]; 726 Casa Bonita Court, Los Altos, CA 94024 (US). **MUSICK, Michael, D.** [US/US]; 916 Southgate Drive, State College, PA 16801 (US). **KEATING, Christine** [US/US]; Box 147, Lemont, PA 16851 (US). **BROWN, Kenneth, R.** [US/US]; 495 Upper Evergreen Drive, Park City, UT 84098 (US).
- (74) Agent: **MONAHAN, Thomas, J.**; The Pennsylvania State University, 200 Innovation Boulevard, 113 Technology Center, University Park, PA 16802-7000 (US).
- (81) Designated States (*national*): AE, AG, AL, AM, AT, AU, AZ, BA, BB, BG, BR, BY, BZ, CA, CH, CN, CR, CU, CZ, DE, DK, DM, DZ, EE, ES, FI, GB, GD, GE, GH, GM, HR, HU, ID, IL, IN, IS, JP, KE, KG, KP, KR, KZ, LC, LK, LR, LS, LT, LU, LV, MA, MD, MG, MK, MN, MW, MX, MZ, NO, NZ, PL, PT, RO, RU, SD, SE, SG, SI, SK, SL, TJ, TM, TR, TT, TZ, UA, UG, US, UZ, VN, YU, ZA, ZW.
- (84) Designated States (*regional*): ARIPO patent (GH, GM, KE, LS, MW, MZ, SD, SL, SZ, TZ, UG, ZW), Eurasian patent (AM, AZ, BY, KG, KZ, MD, RU, TJ, TM), European patent (AT, BE, CH, CY, DE, DK, ES, FI, FR, GB, GR, IE, IT, LU, MC, NL, PT, SE, TR), OAPI patent (BF, BJ, CF, CG, CI, CM, GA, GN, GW, ML, MR, NE, SN, TD, TG).
- Published:**
- With international search report.
  - Before the expiration of the time limit for amending the claims and to be republished in the event of receipt of amendments.
- For two-letter codes and other abbreviations, refer to the "Guidance Notes on Codes and Abbreviations" appearing at the beginning of each regular issue of the PCT Gazette.*

(54) Title: HYDROXYLAMINE SEEDING OF COLLOIDAL METAL NANOPARTICLES

(57) Abstract: Methods for preparing colloidal metal nanoparticles, in which a solution of reductant is added to a boiling solution of a source of metal ion coincidentally with seed colloids are described, including a method using colloidal gold nanoparticle seeds, a gold ion source (HAuCl<sub>4</sub>), and sodium citrate (reductant). Methods for preparing colloidal metal nanoparticles, in which seed colloids are added to a solution of reductant mixed with a solution containing a source of metal ions are also described, including a method in which the seeds are colloidal gold nanoparticles, the source of gold ions is HAuCl<sub>4</sub>, and the reductant is NH<sub>2</sub>OH. Methods for preparing colloidal metal nanoparticles, in which the seed colloids are the result of the application of the previous methods, and the source of metal ions and the reductant are added to the seed colloids in an iterative fashion, are also described. The colloidal metal nanoparticles that are the product of the application of the above methods are also described. Certain colloidal metal nanoparticles have a major axis standard deviation of about 14 % or less, a minor axis standard deviation of about 14 % or less, and an ellipticity < 1.5. Other colloidal metal nanoparticles have major axis standard deviation of about 29 % or less, a minor axis standard deviation of about 20 % or less, and an ellipticity > 1.5.

WO 01/39873 A1

## HYDROXYLAMINE SEEDING OF COLLOIDAL METAL NANOPARTICLES

### FIELD OF THE INVENTION

The present invention relates generally to formation of colloidal metal nanoparticles and films of colloidal metal nanoparticles. In particular, the present invention relates to colloidal metal nanoparticles prepared by hydroxylamine seeding, and monolayers of such  
5 colloidal metal nanoparticles. Further, the present invention relates to the preparation of colloidal metal nanoparticle multilayer films.

### BACKGROUND OF THE INVENTION

The use of nanosized colloidal Au nanoparticles has expanded greatly in recent years.  
10 Whereas ten to fifteen years ago, the predominant use of colloidal Au was in biological transmission electron microscopy, a wide variety of recent papers now describe interesting physical properties and possible applications that extend far beyond imaging. For example, colorimetric DNA sensors based on colloidal Au have been developed. Moreover, organized two-dimensional (2-D) and 3-D arrays of colloidal Au nanoparticles are now occupying the  
15 attention of several groups. Unless one studies metal nanoparticles one at a time, as has recently been described, understanding the behavior of solutions and/or surfaces comprising Au nanoparticles is predicated upon having a single size (and shape) of particle because, in the nanometer regime, almost every relevant physical property of colloidal Au is size-dependent. Photolithography and more recently, nanosphere lithography has been used to  
20 prepare surfaces with highly regular metal features. However, for materials synthesis and for manipulations of these particles in solution, nanoparticles prepared from metal ions in solution comprise the preferred starting materials.

Many different preparations have been reported for the synthesis of colloidal Au, including even some that begin with bulk metal. However, most such preparations begin with  
25  $\text{Au}^{3+}$  and, through use of different reductants, generate particles with a range of particle sizes. For example, reducing agents such as  $\text{NaBH}_4$  or white phosphorous produce small Au particles (diameter  $< 10$  nm) while reductants such as ascorbic acid yield colloidal Au nanoparticles with diameters larger than 10 nm. The most widely-studied reductant is sodium citrate; by varying the citrate:Au ratio, it is possible to prepare colloidal particles with  
30 diameters (d) ranging from 10-150 nm. Unfortunately, for  $d > 30$  nm, the monodispersity

becomes poor and the ellipticity ( $G$ ) – the ratio of the major to minor axis – significantly exceeds unity, the value for a sphere. As a result, these particles are of limited value for nanometer-scale architecture. Indeed, of the many published routes to colloidal Au, none produce large ( $>50$  nm) particles with good monodispersity. Their utility is further restricted by the low particle concentrations generated by these methods. For example, EP 426300B1 describes 2.6-nm diameter colloidal Au nanoparticles ("seeds") prepared by  $\text{BH}_4^-$  reduction grown to larger sizes by addition of a boiling solution of  $\text{HAuCl}_4$  and citrate. This approach produces large colloidal Au particles more predictably and reproducibly than citrate reduction, but because the seeds are highly polydisperse (40% standard deviation), the monodispersity is comparable.

Formation of conductive metal films by faradaic and non-faradaic deposition onto immobilized metal nanoparticles is a widely-used process in industry, and of significant recent interest. The focus of this work has typically been on production of thin films exhibiting high conductivity and good adhesion, with special attention given to micron-to-submicron control of film thickness and ease of fabrication. Though largely successful, two aspects of film growth by electroless metal deposition have received little attention. The first is that the number of metal nanoparticles used to nucleate film growth is usually not a controllable parameter. As a result, detailed mechanistic information about particle coalescence is lacking. The second is that the analogous processes in solution – that is, enlargement of suspended metal nanoparticles – have not been studied. As a result, information about the size and shape of growing particles is unavailable.

Accordingly, there remains a need for metal nanoparticles with narrow size distributions, and methods for making them. There also remains a need for methods for controlled growth of nanoparticles in Au colloid monolayers, multilayers, and in solution, along with the control of desired physical characteristics of such monolayers, multilayers, and solutions.

Ensembles of nanoparticles display unique optical and electrical properties that are distinct from their respective bulk properties or simply the average measurement of individual particles. To a large extent, however, bulk material properties (i.e., catalytic, optical, electrical, biocompatibility) are determined by nanoscale features. The ability to tune particle, size, shape, chemical composition, array geometry and linking chemistries provides a flexible platform to manipulate material properties through rational design of the principal components (i.e., metal or semiconductor nanoparticles).

Materials composed from 2-D and 3-D ensembles of nanoparticles are becoming increasingly important in analytical and materials chemistries; indeed, practical applications in nanoelectronic and optoelectronic devices, chemical sensors, and catalysis seem imminent. For example, arrays of crystalline modified polystyrene spheres and suspended ensembles of ligand-coated metal nanoparticles are finding use as vapor phase molecular recognition sensors. Self-organized 2-D nanoparticle superlattices of latex spheres, CdS, CdSe, Au, and Ag structures have been constructed and analyzed. Organized 3-D arrays of nanoparticles with inter- and intra-layer particle registry have been assembled from polystyrene, Ag, CdS, and inorganic oxide nanoparticles. However, with the exception of the inorganic oxides reported by Stein and coworkers, see Holland, et al., *Chem. Mater.* 1999, 11:795-805; and Holland, et al., *Science* 1998, 281:802-804, no assemblies extend more than a few layers above the substrate and none offer any control over film thickness.

Multilayers of nanoparticles produced by alternate immersion into a bifunctional crosslinker and nanoparticle solutions produce random arrays of nanoparticles of controllable thickness. Particle spacing of films grown "stepwise" or "layer-by-layer" are determined by the molecular size of the crosslinker. In this fashion, assemblies of dithiol-linked Cu and polyion linked CdS and SiO<sub>2</sub> have been characterized. Multilayers of thiol-capped Au nanoclusters were described separately by the Schiffrin and Murray groups, see Bethell et al., *Electroanal. Chem.* 1996, 409:137-143; Baum, et al., *Langmuir* 1999, 15:866-871; Fink, et al., *Chem. Mater.* 1998, 10:922-928; Hostetler, et al., *J. Am. Chem. Soc.*, 1996, 118:4212-4213; Terrill, et al., *J. Am. Chem. Soc.* 1995, 117:1253-1254; and the optical, electrical, and electrochemical properties of thiol-linked 12-nm diameter Au colloids have been described by the Natan group, see, Musick, et al., *Langmuir* 1999, 15:844-852; and Musick, et al., *Chem. Mater.* 1997, 9:1499-1502. Shipway, et al., *Chem. Mater.* 1999, 11:13-15, have constructed an electrochemical sensor based on donor-acceptor chemistry where hydroquinone, a  $\pi$ -acceptor, is concentrated in the Au colloid multilayer by bipyridinium cyclophane, a  $\pi$ -donor used as "molecular glue". Sarathy, et al., *J. Phys. Chem. B.* 1999, 103:399-401 characterized superlattices formed via layer-by-layer deposition of Pt, CdS, and Au nanoparticles by x-ray diffraction. Likewise, nanoparticles have been encapsulated in sol-gel and aerogel matrices for evaluation as nonlinear optical materials or prospective catalysts. Other advances in nanoparticle assembly include the temperature dependent assembly/disassembly of oligodeoxyribonucleotide-Au colloid conjugate networks and the construction of 1-D arrays

of Au-poly(pyrrole) nanoparticle arrays via membrane pore template synthesis, potentially a unique method to construct single-electron devices from solution.

Interest in 2-dimensional metal (2-D) nanoparticle arrays stems from several unique characteristics. (i) Concentrated solutions of monodispersed Au nanoparticles from 2-100 nm in diameter are easily synthesized. Metal nanoparticles readily adsorb onto appropriately derivatized surfaces. Typically, organosilanes, hyperbranched polymers, or alkylthiols are used to generate arrays with random packing but with a reproducible overall coverage and with a reasonable distribution of interparticle spacing. (ii) Optical properties are a function of particle spacing, size, and composition, easily tailored attributes. (iii) Particles have a high surface area, useful for applications in catalysis, electrochemistry, biomolecule conjugation, and surface-sensitive spectroscopies. In contrast to sol-gel or polymer encapsulation, where the majority of the particle is coupled to the matrix and inaccessible to solution or gas phase chemistry, only a small fraction of an individual particle is in contact with the surface. (iv) Fabrication of patterned collections of nanoparticles has potentially important implications in nanoelectronic device fabrication and biosensing. In this regard, Natan and coworkers have previously characterized Au colloid monolayer synthesis, rate of assembly, thermodynamics, and morphology; extension of assemblies into 3-D architectures may lead to new properties and broadened applications. See Grabar, et al., *Anal. Chem.* 1995, 67:735-743; Grabar, et al., *Langmuir* 1996, 12:2353-2361; Grabar, et al., *J. Am. Chem. Soc.* 1996, 118:1148-1153; Keating, et al., *J. Chem. Educ.* 1999, 76:949-955; and Grabar, et al., *J. Anal. Chem.* 1997, 69:471-477.

Accordingly, there remains a need for the development of a general methodology for assembling bulk metal-like films directly from solution in a stepwise fashion. The present invention overcomes the limitations of the prior art and further illustrates possible applications in electrochemistry, biosensors, conductive coatings, surface patterning, and optical devices.

## SUMMARY OF THE INVENTION

The present invention provides a method for preparing colloidal metal nanoparticles, in which a solution of reductant is added to a boiling solution of a source of metal ion coincidentally with seed colloids. In a preferred embodiment, the colloidal metal nanoparticles are colloidal gold nanoparticles, the source of gold ions is  $\text{HAuCl}_4$ , and the reductant is sodium citrate. The present invention is also directed toward a method for

preparing colloidal metal nanoparticles, in which seed colloids are added to a solution of reductant mixed with a solution containing a source of metal ions. In a preferred embodiment, the colloidal metal nanoparticles are colloidal gold nanoparticles, the source of gold ions is  $\text{HAuCl}_4$ , and the reductant is  $\text{NH}_2\text{OH}$ . In a further embodiment, the seed colloids are the result of the application of the method, and the source of metal ions and the reductant are added to the seed colloids in an iterative fashion. The present invention is also directed to the colloidal metal nanoparticles that are the product of the application of the above methods. In one embodiment, colloidal metal nanoparticles have a major axis standard deviation of about 14% or less, a minor axis standard deviation of about 14% or less, and an ellipticity < 1.5. In another embodiment, colloidal metal nanoparticles have a major axis standard deviation of about 29% or less, a minor axis standard deviation of about 20% or less, and an ellipticity > 1.5.

The present invention is also directed toward a method for enlarging immobilized gold nanoparticles using a similar method of immersing an Au colloid monolayer in a solution of reductant, and adding a solution having a source of  $\text{Au}^{3+}$ . The present invention is also directed towards methods for the preparation of thin gold films whose nanostructure can be varied based on the amount of coverage of Au colloid in the monolayer. In the case of a low-coverage Au colloid monolayer, a gold film with features up to about 50 nm tall and about 75 nm wide results. In the case of a high-coverage Au colloid monolayer, a gold film with features about 25 nm tall or less results.

The present invention is also directed toward the gold films prepared by these methods, including a thin Au film having substantially similar conductivity to pure Au, a thin Au film useful as an a cyclic voltammetry electrode, a thin Au film whose nanostructure is indistinguishable from those of granular metal films prepared by evaporation, and having a mean roughness of about 3 nm rms, a thin Au film with increased SERS intensity, a thin Au film for which a reflectivity vs. excitation angle plot exhibits a pronounced minimum.

The present invention is also directed toward a method for preparing a gold film multilayer an Au colloid multilayer is immersed in a solution of reductant, followed by addition of a solution containing a source of  $\text{Au}^{3+}$ .

#### BRIEF DESCRIPTION OF THE FIGURES

Figure 1 shows a comparison of  $\lambda_{\max}$  (top), ellipticity (G) (middle), and peak width at half-max (PWHM) (bottom) versus major axis diameter for colloidal Au nanoparticles prepared by direct citrate reduction of  $\text{Au}^{3+}$  ( $\square$ ) and by citrate-based seeding of 2.6-nm diameter ( $\square$ ) and 12-nm diameter ( $\bullet$ ) colloidal Au.

Figure 2 shows optical spectra for solutions of 19-, 25-, and 53-nm diameter Au nanoparticles grown by citrate seeding of 12-nm diameter colloidal Au. Size and shape data for these particles are described in Table 1.

Figure 3 shows optical spectra (0.1-s integration time) of a mixture of 3.2 ml of 0.01%  $\text{HAuCl}_4$ /0.1 ml of 40 mM  $\text{H}_2\text{NOH}$  after 20 minutes (a), and 1 (b), 6 (c), 11 (d) and 56 seconds (e) after addition (without stirring) of 0.050 ml of 17 nM, 12-nm diameter colloidal Au.

Figure 4 shows absorbance at 526 nm measured every second (0.1-s integration time) after additions of 0.1 ml of 0.1 %  $\text{HAuCl}_4$  (at the times indicated) to an unstirred mixture of 3.2 ml of 0.01 %  $\text{HAuCl}_4$ /0.1 ml of 40 mM  $\text{H}_2\text{NOH}$ /0.050 ml of 17 nM, 12-nm diameter colloidal Au.

Figure 5 shows the iterative seeding scheme used to produce the colloids shown in Table 2.

Figure 6 is an enlarged TEM image of 4th-iteration  $\text{NH}_2\text{OH}$ -seeded colloidal Au (panel E in Figure 6).

Figure 7 shows optical spectra in  $\text{H}_2\text{O}$  of a 12-nm diameter Au colloid monolayer on APTMS-coated glass as prepared (a), and after immersion in 0.01  $\text{HAuCl}_4$ /4 mM  $\text{NH}_2\text{OH}$  for 10 (b), 20 (c), 30 (d), 40 (e), 50 (f), 60 (g), 120 (h), 300 (i), 900 (j), 1500 (k), and 2700 seconds (l).

Figure 8 in the top panel shows representative optical spectra for 12-nm diameter Au colloid monolayers on APTMS- (a) and MPTMS-coated glass (b). The middle panel shows UV-Vis-near-IR spectra for seven 12-nm diameter Au colloid monolayers on APTMS/glass after exposure from 1 to 8 minutes to 0.01 %  $\text{HAuCl}_4$ /0.4 mM  $\text{NH}_2\text{OH}$ . The bottom panel shows UV-Vis-near-IR spectra for seven 12-nm diameter Au colloid monolayers on MPTMS/glass after exposure from 1 to 30 minutes to 0.01 %  $\text{HAuCl}_4$ /0.4 mM  $\text{NH}_2\text{OH}$ .

Figure 9, at the top, shows cyclic voltammograms at three different scan rates of 5 mM  $[\text{Ru}(\text{NH}_3)_6]\text{Cl}_3$ /0.1 M  $\text{Na}_2\text{SO}_4$  at a colloidal Au film (12-nm diameter colloidal Au monolayer/APTMS/glass immersed in 0.01%  $\text{HAuCl}_4$ /0.4 mM  $\text{NH}_2\text{OH}$  in an orbital shaker at 120 rpm for 17 minutes), and, in the bottom panes, shows comparison of 100-mV/s cyclic

voltammograms of the same electrolyte taken at colloidal Au monolayers seeded (as above) for 3, 8, and 17 minutes.

Figure 10 shows AFM images ( $1\ \mu\text{m} \times 1\ \mu\text{m}$ ) of a 12-nm diameter Au colloid monolayer on MPTMS-coated glass (A), and after shaking in an orbital shaker at 120 rpm in a solution of 0.01%  $\text{HAuCl}_4/0.4\ \text{mM}\ \text{NH}_2\text{OH}$  for 3 (B), 6 (C), 7 (D), 9 (E), and 30 minutes (F).

Figure 11 shows AFM images ( $1\ \mu\text{m} \times 1\ \mu\text{m}$ ) of a 12-nm diameter Au colloid monolayer on APTMS-coated glass (A), and after shaking in an orbital shaker at 120 rpm in a solution of 0.01%  $\text{HAuCl}_4/0.4\ \text{mM}\ \text{NH}_2\text{OH}$  for 2 (B), 3 (C), 5 (D), 8 (E), and 17 minutes (F).

Figure 12 shows FE-SEM images of  $\text{Au}/\text{NH}_2\text{OH}$ -enlarged Au colloid monolayers.

Images A and C correspond to samples imaged by AFM in Figure 5, Panels C and F, respectively; images B and D correspond to samples imaged by AFM in Figure 4, Panels C and F, respectively.

Figure 13 shows SERS spectra of 10 mM BPE in 9:1  $\text{H}_2\text{O}:\text{CH}_3\text{OH}$  drop-coated on 12-nm diameter Au colloid monolayers on APTMS-coated glass as prepared (a) and after exposure to 0.01 %  $\text{HAuCl}_4/0.4\ \text{mM}\ \text{NH}_2\text{OH}$  for 1 (b), 6 (c) and 17 minutes (d). Acquisition parameters: 23 mW of 632.8-nm photons at the sample, integration time = 1 s,  $\approx 8\ \text{cm}^{-1}$  bandpass.

Figure 14, in the top panel shows a simulated SPR curve for a 50-nm thick evaporated Au film on glass and observed SPR curves for a 12-nm diameter Au colloid monolayer/APTMS/glass substrate and a 12-nm diameter Au colloid multilayer substrate (Au colloid monolayer on MPTMS-coated glass with seven additional colloidal layers added using 2-mercaptoethylamine as a bifunctional cross-linker"). The middle panel shows SPR curves for high and low coverage 12-nm diameter Au colloid monolayers on organosilane-coated glass after 10 minutes of shaking in an orbital shaker (at 120 rpm) in a solution of 0.01 %  $\text{HAuCl}_4/0.4\ \text{mM}\ \text{NH}_2\text{OH}$ . The bottom panel shows SPR curve for the Au colloid multilayer of the top panel after the  $\text{HAuCl}_4/\text{NH}_2\text{OH}$  treatment described for the middle panel.

Figure 15 shows optical absorbance spectra for Au/Ag mixed-nanoparticle multilayers with exposures to either Au (11-nm diameter, 17 nM, 60 min) or Ag colloid and  $\text{HSCH}_2\text{CH}_2\text{OH}$  (5 mM, 10 min) wet (top) and dry (bottom). The film composition is; (a) Au monolayer; (b) Au/Ag; (c) Au/Ag/Ag; (d) Au/Ag/Ag/Ag/Au; (e) Au/Ag/Ag/Ag/Au/Ag; (f) Au/Ag/Ag/Ag/Au/Ag/Au.



Figure 16 is a tapping mode AFM (scan size 1  $\mu\text{m}$  x 1  $\mu\text{m}$ ) of HSCH<sub>2</sub>CH<sub>2</sub>OH-linked Au colloid multilayers: (A) monolayer; (B) 3 Au treatments; (C) 5 Au treatments; (D) 7 Au treatments; (E) 11 Au treatments.

Figure 17 shows absorbance at 518 nm for 2-mercaptoethanol-linked Au colloid multilayers versus particle coverage (8). The solid line is the least-squares fit ( $r=0.980$ ) to data on dry samples; the dashed line is the least-squares fit ( $r=0.979$ ) to wet samples.

Figure 18 shows Uv-vis absorbance spectra of HRP-linked Au colloid multilayers as a function of colloidal Au/HRP layers. The inset is a plot of the enzymatic activity of the HRP-linked films with increasing number of colloidal Au/HRP layers.

Figure 19 shows Uv-vis/near-IR transmission spectra of 12-nm diameter Au colloid multilayers crosslinked with 1,4-Diisocyanobenzene (1), 4,4'-Diisocyanato-*p*-biphenylene (2), and 4,4'-Diisocyanato-*p*-terphenylene (3).

Figure 20 shows volume fractions of 2-mercaptoethanol linked Au colloid multilayers determined by theory ( $\square$ ) and different experimental methodologies: from the maximum film ( $\square$ ) and minimum film ( $\square$ ) depths as determined by atomic force microscopy, and from a combination of atomic absorbance spectrometry and AFM ( $\square$ ).

Figure 21 shows DC resistance of 2-mercaptoethylamine ( $\square$ ), 1,6-hexanedithiol ( $\square$ ), and 2-mercaptoethanol (+) linked 12-nm diameter Au colloid multilayers

Figure 22 shows DC resistance immobilized colloidal Au (11-nm diameter) multilayers linked by 1 ( $\square$ ), 2 ( $\square$ ), and 3 ( $\square$ ).

Figure 23 shows electrostatic force microscopy (left) images and AFM images (right) of 12-nm diameter Au MEA linked colloid multilayers (number of layers indicated on graph). EFM images collected at 2 V at 1 Hz scan rate with a lift height of 25 nm.

Figure 24 shows surface plasmon resonance curves of a 39-nm thick Au film (—), and identical films treated with one (---), two ( $\cdot\cdot\cdot$ ) and three (----) successive exposures to 1.0 mM MEA in CH<sub>3</sub>CH<sub>2</sub>OH and 17 nM 12-nm diameter colloidal Au.

Figure 25. Effect of UV exposure upon SERS spectra for BPE adsorbed to a multilayer surface comprising 9 layers of Ag particles crosslinking by 2-mercaptoethanol. Spectra shown are for 10 mM BPE (A), the as-prepared multilayer surface in 10 mM BPE (B), and for the same surface in 10 mM BPE following exposure to UV radiation for 2 min. (C), and 5 min. (D). Conditions: 107 mW of 647.1 nm excitation at the sample, 5  $\text{cm}^{-1}$  bandpass, 1.0-s integration x 10 accumulations.

## DETAILED DESCRIPTION OF THE INVENTION

Many of the examples and embodiments herein describe the use of colloidal Au nanoparticles, but it is to be understood that any other metal (including alloys and mixtures of metals) is also contemplated by and within the scope of the invention. For example, metals include but are not limited to Ag, Cu, Al, or alloys comprised of two or more of Au, Al, Ag, and Cu. In other embodiments, the metal nanoparticles comprise a core of Ag, Al, Au, or Cu (or an alloy of two or more of these metals) substantially covered by a shell of any metal, any oxide, any sulfide, any phosphide, or any organic or inorganic polymer. In addition, although preferred embodiments employ metal nanoparticles that are substantially spherical, it is to be understood that other shapes are also contemplated. The glass may be of any type. Examples of suitable glasses include, but are not limited to SF11 glass slides (Schott Glass Technologies) BK7 microscope slides (Fisher Scientific), and glass coverslips (Fisher Scientific).

## CONTROL OF PARTICLE SIZE AND SHAPE BY SEEDING OF COLLOIDAL AU NANOPARTICLE SOLUTIONS

The use of more monodisperse seeds (e.g.  $12 \pm 1.5$  nm diameter) yields larger particles and particles with narrower size distributions. A superior new synthetic protocol is described, based on room-temperature seeding of colloidal Au by  $\text{NH}_2\text{OH}/\text{Au}^{3+}$ . This method is consistent and reproducible enough to predict, *a priori*, final colloidal diameters within a few nanometers. Iterative seeding using this approach can be used to rapidly produce large colloidal Au nanoparticle solutions that exhibit excellent monodispersity. Interestingly, repetitive seeding with  $\text{NH}_2\text{OH}$  leads to formation of a small percentage of cylindrical, high aspect-ratio rods. Note that such rods have been generated electrochemically in the pores of membranes.

The present invention includes the preparation and characterization of conductive Au films prepared by controlled growth of the nanoparticles in Au colloid monolayers and multilayers using aqueous solutions of  $\text{NH}_2\text{OH}/\text{HAuCl}_4$ . Formation of conductive metal films by faradaic and non-faradaic deposition onto immobilized metal nanoparticles is a widely-used process in industry.

$\text{NH}_2\text{OH}$ -mediated reduction of  $\text{Au}^{3+}$  is an excellent route to enlargement of immobilized 12-nm diameter colloidal Au nanoparticles tethered to organosilane-coated glass

substrates. By using low concentrations of  $\text{Au}^{3+}$  (added as  $\text{HAuCl}_4$ ), it is possible to monitor and control the rate of particle growth and coalescence. Immersion of Au colloid monolayers for just a few minutes into a shaken flask containing 0.01%  $\text{HAuCl}_4$ /0.4 mM  $\text{NH}_2\text{OH}$  leads to evolution of optical properties very similar to those of evaporated Au films near the insulator-conductor threshold; additional exposure leads to metallic thin films with DC resistances as low as 1-10  $\Omega$ , allowing them to be used for cyclic voltammetric measurements. Investigation of film nanostructure using atomic force microscopy (AFM) and field-emission scanning electron microscopy (FE-SEM) indicates that enlarged particles are neither spherical nor cylindrical, but rather have a highly complex shape. Not surprisingly,  $\text{NH}_2\text{OH}$ -mediated particle enlargement leads to dramatic improvements in SERS enhancement factors. Nanoscale morphology of conductive films depends critically on the initial coverage of 12-nm diameter Au nanoparticles, and SPR measurements are acutely sensitive to such differences, even in films exhibiting ostensibly identical bulk optical and electrical properties.

Particle seeding appears to be a valuable addition to the synthetic repertoire for colloidal Au, both for the production of large particles with improved monodispersity and for fabrication of high-aspect ratio colloidal Au rods. Both boiling citrate and room-temperature hydroxylamine served effectively as reductants for 2.6- and 12-nm diameter colloidal Au seeds. For hydroxylamine, iterative seeding can be used to grow (from 12-nm diameter seeds) particles with 100-200 nm major axes.

As part of a study aimed at preparation of protein: Au colloid complexes, a thorough study of the physical properties Au nanoparticles made by the Frens method (i.e. direct reduction of  $\text{Au}^{3+}$  by citrate) has been published; Gooman, Faulk, et al., *Immunohem.* 1971, 8:1081-83; Horisberger, *Biol. Cell.* 1979, 36:253-58; Hayat, Ed., *Colloidal gold: Principles, Methods, and Applications*; Academic Press: San Diego, 1989, vol. 1-2; Beesley, *Colloidal Gold: A New Perspective for Cytochemical Marking*; Oxford University: Oxford, 1989; Vol. 17; each specifically incorporated by reference. By varying the citrate: $\text{Au}^{3+}$  ratio, Au nanoparticles with diameters from 10-70 nm were prepared and characterized by TEM and UV-Vis spectrophotometry. Four parameters were used to describe each preparation of colloid: the wavelength of maximum absorbance ( $\lambda_{\text{max}}$ ) and peak width at half max (FWHM) from the UV-Vis data, and the mean particle diameter (d) and ellipticity (G) from TEM data. Due to the asymmetry of the colloidal Au surface plasmon band, FWHM is defined

straightforwardly as twice the difference between  $\lambda_{\max}$  and the  $\lambda$  of half-maximal absorbance to the red of the  $\lambda_{\max}$ .

In contrast, the mean particle diameter  $d$  is an oversimplification in that no colloidal Au particles are purely spherical: TEM images show the presence of major and minor axes (the ellipticity  $G$  is the ratio major:minor axial ratio). Accordingly, while  $d$  is used herein in reference to the dimensions of the major axis, all particles are described by mean major and minor axes (e.g. Table 1). The TEM images only two of the three dimensions in a particle, and it is assumed that the dimensions of the third are the same as one of the two imaged. The particles may also be prolate (cigar-shaped; third axis = minor) or oblate (pancake-shaped; third axis = major). While Goodman, et al., *J. Microsc.* 1981, 123:210-13, state that colloidal Au nanoparticles are oblate, both logic and experiment suggest that the reverse is true: particles on TEM grids adsorb so as to maximize their contact with the surface, meaning the axis normal to the surface must be minor. Since minor and major axes are seen in TEM images, there must be two minor axes, making the particles prolate. In accord with this reasoning, atomic force microscopy images of Au nanoparticles on glass slides known to have axes of 40 and 30 nm indicates the tops of the particles are 30 nm above the surface.

The  $d$ ,  $G$ ,  $\lambda_{\max}$  and PWHM for Au nanoparticles made by the Frens method have been compared to those prepared by seeding (Figure 1 and Table 1).

In the approach described in EP 426300B1, the dimensions of existing Au nanoparticles (the "seeds") are increased by mixing with additional reductant (i.e. citrate) and  $\text{Au}^{3+}$ . In practice, a mixture of citrate and colloidal Au is added to a solution of boiling, dilute  $\text{HAuCl}_4$  in  $\text{H}_2\text{O}$ . What is important for this method is the relative rate of new particle formation (via  $\text{Au}^{3+}$  reduction) in solution versus the rate of  $\text{Au}^{3+}$  reduction on the surface of existing particles. If the latter is much greater than the former, then particle growth will occur at the expense of new particle nucleation. From previous work, it is well-appreciated that reduction of  $\text{Au}^{3+}$  on *any* small particles is rapid, explaining the need for filtered solutions and scrupulously clean glassware for the production of colloidal Au. New particle nucleation can be therefore be averted by seeding. The absence of new particle nucleation is especially critical for growth of large particles, because in the Frens method, as particles are growing larger, new (small) particles can be forming.

Several trends are seen in the plots of  $\lambda_{\max}$ , ellipticity, and peak width at half maximum (PWHM) versus particle diameter for colloidal Au made by Frens' method and by

seeding using 2.6-nm diameter and 12-nm diameter seeds (Figure 1). For each type of particle,  $\lambda_{\max}$  increases with increasing size, although not dramatically. Increasing the diameter of a colloidal Au nanoparticle from 19 nm to 53 nm, nearly a factor of three, leads only to a 14 nm red shift in  $\lambda_{\max}$  (Figure 2); red shifts of 150 nm or more can be realized by aggregation of small particles; however, increasing particle diameters lead to increasing ellipticities and to significantly broadened optical spectra. The latter has been shown to result in large part from Rayleigh light scattering from particles with diameters  $\geq \lambda/20$ . It should be noted that because light scattering is so sensitive to particle diameter, PWHM can be used as a rapid diagnostic for the quality of citrate-derived, small diameter colloidal Au preparations. For example, preparations of 12-nm diameter colloidal Au with PWHM  $>85$  nm invariably exhibit roughly twofold higher standard deviations in  $d$  than those with PWHM  $<85$  nm.

Comparison of the physical properties of colloidal Au prepared by seeding with that made by direct citrate reduction indicates the superiority of the former (Table 1). In particular,  $G$  is significantly greater for colloidal Au made by direct citrate reduction: several batches clustered around  $d = 40$  nm all had  $G \geq 1.3$ , while the analogous particles made by seeding exhibited  $G$  values  $\approx 1.2$ . Even particles in the 20-30 nm diameter range made by direct citrate reduction were more elliptical than the corresponding seeded particles. Moreover, PWHM for seeded particles are consistently lower than for particles made by direct citrate reduction. For the three sizes of 12-nm seeded particles shown in Figure 2, the PWHM are nearly identical, and the only significant difference is the aforementioned shift in  $\lambda_{\max}$ . Colloidal Au solutions made by direct citrate reduction exhibit broadened PWHM over the entire range of particle diameters.

In theory, the high degree of ellipticity in colloidal Au made by direct citrate reduction arises from two components: differential reduction rates at sites on the particle, and differential diffusion to parts of the particles. High-resolution TEM studies have shown the presence of crystalline faces in small colloidal Au nanoparticles. If reduction of  $\text{Au}^{3+}$  is substantially faster (or slower) on certain faces than on others, then anisotropic particle growth will occur. In this regard, Weisner & Wokaun, *Chem. Phys. Lett.* 1989, 157:569-75, have shown that under certain conditions, highly anisotropic colloidal Au nanoparticles can be prepared; likewise, production of cubic colloidal particles has also been described. Another factor that could favor elliptical particles is the enhanced amount of  $\text{Au}^{3+}$  reaching the ends of the ellipse: flux to a hemisphere is enhanced relative to flux to a plane. While this factor is

more important in unstirred solutions, even in stirred solutions it could contribute to increased growth at the hemispherical "ends" of a prolate spheroidal particle.

The standard deviations of the axial dimensions are substantially lower for particles seeded with 12-nm diameter colloidal Au than for particles made by direct citrate reduction or 2.6-nm diameter seeding. For example, in batch number 9 of the particles made by direct citrate reduction (Table 1), the major axis is  $56 \pm 8.4$  nm. For small seeds of the corresponding size (batch number 5)  $d = 56 \pm 7.2$  nm, while for batch number 8 of the large seeds,  $d = 53 \pm 4.8$  nm. The lower dispersity in particle size for 12-nm seeded particles becomes even more significant for larger particles (e.g., large seed batch number 9 vs. small seed batch number 6, large seed batch number 10 vs. small seed batch number 7).

The increased dispersity in particle size for particles made using 2.6-nm diameter seeds reflects the poor monodispersity and increased ellipticity of the seeds themselves (Table 1). The 2.6-nm diameter colloidal particles have  $\approx 1$ -nm standard deviations in diameter. While this is about the same absolute standard deviation in diameter measured for good preparations of 12-nm diameter particles, it is quite large as a percentage of particle size. Furthermore, the measured ellipticity is 1.3 (versus 1.1 for 12-nm diameter particles). Accordingly, seeding with 2.6-nm particles leads to more dispersion in particle size, reflected by larger standard deviations in diameter and by very substantial increases in peak widths (Table 1).

In short, citrate seeding 12-nm diameter colloidal Au nanoparticles yields sols with improved physical properties relative to direct particle production by citrate reduction of  $\text{Au}^{3+}$  or by seeding with 2.6-nm diameter seeds. The disparity in quality of colloidal preparations is especially prevalent for  $d > 40$  nm.

#### Hydroxylamine Seeding

Drawbacks of citrate seeding include the need for boiling  $\text{H}_2\text{O}$  and the need to keep the  $\text{Au}^{3+}$  and the reductant apart; ideally, seeding could be carried out at room temperature, and initiated upon introduction of seeds to premixed solutions of  $\text{Au}^{3+}$  and reductant (or introduction of  $\text{Au}^{3+}$  to a mixture of reductant and seeds). This can be accomplished by a process with a solution nucleation rate constant of zero at room temperature and a surface nucleation rate constant significantly greater than zero at room temperature. In Au electroless metal plating, these requirements are satisfied by chelation of  $\text{Au}^+$  to cyanide, which moves

the solution reduction potential too far negative for formation of AuO, so that only adsorbed Au<sup>+</sup> ions is possible. Similarly, the reductant hydroxylamine (NH<sub>2</sub>OH) has been shown to favor reduction of Au ions at metallic Au surfaces at room temperature over reduction in solution, and the application of NH<sub>2</sub>OH seeding to colloidal Au nanoparticles has been described in a preliminary fashion in we have described in a preliminary fashion in Brown & Natan, *Langmuir* 1998, 14:726-728.

At room temperature, mixtures of NH<sub>2</sub>OH and Au<sup>3+</sup> (added as HAuCl<sub>4</sub>) do not lead to formation of colloidal Au nanoparticles in solution. Thus, the optical spectrum of a mixture of 0.01 % HAuCl<sub>4</sub> and 40 mM H<sub>2</sub>NOH is featureless after 20 minutes (spectrum a of Figure 3). Addition of 50 µl of a solution containing 12-nm diameter colloidal Au seeds leads immediately to significant growth in the intensity of the colloidal Au surface plasmon band (spectra b - e in Figure 3). Changes in the optical spectra are essentially complete after 11 seconds, since a spectrum recorded after 56 seconds is essentially identical, as are spectra recorded every five seconds between these times (data not shown). Since the formation of new particles is precluded by the control experiment described by spectrum a, the spectral changes suggest enlargement of the seed particles. If so, cessation in particle growth must result from depletion of Au<sup>3+</sup>.

This notion is confirmed by the data in Figure 4, which plots the absorbance at 526 nm over time as aliquots of HAuCl<sub>4</sub> are added to a pre-reacted mixture of 0.01% HAuCl<sub>4</sub>, NH<sub>2</sub>OH, and 12-nm diameter colloidal Au. At t = 0, the absorbance A ≈ 1, indicating that the Au<sup>3+</sup> already in solution has already been consumed to enlarge the 12-nm diameter colloidal Au particles. After addition of Au<sup>3+</sup>, there is a nearly instantaneous increase in absorbance, followed by a slight decrease and then a leveling off. Each subsequent addition of Au<sup>3+</sup> leads to an increase in absorbance, and to a new (higher) level. Thus, HAuCl<sub>4</sub> can be made the limiting reagent in NH<sub>2</sub>OH-seeded growth of 12-nm diameter colloidal Au: introduction of a known quantity of Au<sup>3+</sup> to a solution containing colloidal Au nanoparticles and an excess of NH<sub>2</sub>OH leads to particle growth, until the Au<sup>3+</sup> is consumed.

This method of seeded particle growth is valuable in three respects. First, particle enlargement can be carried out at room temperature. Second, since Au<sup>3+</sup> can be made limiting, particles may be grown to a pre-specified size. Finally, NH<sub>2</sub>OH/Au<sup>3+</sup> seeding is well-suited for growth of immobilized Au nanoparticles, because a colloidal Au-derivatized surface can be easily immersed into a solution of HAuCl<sub>4</sub>/NH<sub>2</sub>OH.

A TEM image of colloidal particles produced by a  $\text{NH}_2\text{OH}/\text{Au}^{3+}$  seeding procedure analogous to that described for the data in Figure 3 was obtained. Two aspects of the image are notable: the excellent monodispersity of the spherical particles ( $51 \pm 5.2 \text{ nm} \times 46 \pm 4.7 \text{ nm}$ ), and the presence of a distinct population (5-10%) of colloidal Au rods ( $141 \pm 38 \text{ nm} \times 31 \pm 4.6 \text{ nm}$ ) with ellipticities far greater ( $\approx 4.5$ ) than any particles derived from citrate reduction of  $\text{Au}^{3+}$ , whether seeded or not. The standard deviation of the major and minor axes of the spherical particles appears equivalent to that produced by citrate seeding with 12-nm diameter colloidal Au. In contrast, the length of the rods' major axis is highly variable, ranging from 90 nm to  $>200 \text{ nm}$ , while the rods' minor axes shows the same small standard deviation (4.7 nm) as the spherical particles. More importantly, the minor axis is more than three standard deviations shorter than the minor axis of the dominant population, suggesting that the rods do not form by fusion of spheres.

Iterative, stepwise seeding favorably impacts the size and shape distribution of the spherical particles. Figure 1 and Table 1 show clearly that single-step enlargement of 2.6-nm or 12-nm diameter colloidal Au particles diameters below 40 nm is well-behaved; for larger particles, the PWHM and ellipticity seem to rise exponentially. Growing large particles in multiple steps leads to minimization of these effects.

The results of an iterative seeding experiment as performed in Figure 5 are described in Table 2, which gives a detailed particle size analysis. Spherical particles spanning nearly an order of magnitude in size ( $\approx 12\text{-}13 \text{ nm}$  to over  $100 \text{ nm}$ ) resulted. Colloidal Au rods are definitely not fused or aggregated spheres. This is easily confirmed by examination of Figure 6, which shows that the rods are solid and are significantly smaller in the minor axis than surrounding quasi-spherical particles. Another interesting point that can be gleaned from Figure 6 is that none of the rods are blunt-ended: both ends are hemispherical, some almost perfectly so. The second clear finding is that there is no continuum from spherical to rod-shaped particles; rather, there are two distinct populations, with nothing in between. In an exemplary population, the transition from  $G < 1.5$  to  $G > 1.5$  is extremely abrupt, with a two order-of-magnitude difference in particle populations. In one example where particles had a mean diameter of 41 nm, early 3000 of 3300 particles had a  $G$  close to 1, and the remainder had  $G$  values from 2 to as high as 8.

Table 2 gives size statistics for both particle shapes individually and for the total set of particles, from which several key points are revealed. (i) Comparison of the median and mean



values is provided to show that for samples containing a bimodal sample distribution, the statistical mean differs from the median value of the set. Likewise, the proximity of the median and mean values in small colloidal particle sets demonstrate that in a uniform particle set these two values should be close. (ii) The standard deviation (SD) of the axial dimensions also climbs very quickly. Once the rods are dropped from consideration, the SD for the remaining population drops dramatically and the median and mean values come into close agreement. (iii) Neither the 12 nm or the next larger colloid shows evidence of colloids with high G; the dominant population is spherical. However, the minor axis of the rods is substantially smaller than the minor axis of spheres in the same batch. Thus, the growth of 12 nm seed particles into rods must be a process that is not simply limited to an accelerated growth in one dimension but a reduced growth rate in the other two axial directions.

Given that suspensions of large (>50 nm diameter) Au nanoparticles could be prepared by seeding of pre-formed, 12 nm diameter colloidal Au solutions with  $\text{Au}^{3+}$  and  $\text{NH}_2\text{OH}$  in solution, the same reaction was performed with immobilized Au colloid monolayers and multilayers, with three synthetic goals. (i) Theory predicts that large-diameter colloidal Au particles are more active for surface enhanced Raman scattering (SERS) than smaller ones; however, in current approaches to SERS-active substrates based on self-assembly colloidal Au or Ag particles from solution, only low concentrations of large Au nanoparticles can be stably prepared, and the diffusion coefficient is inversely proportional to the particle radius. Thus, manufacture of SERS substrates by self-assembly of, e.g., 50-nm diameter colloidal Au particles is laborious. (ii) The insulator-conductor transition in discontinuous or semi-continuous Au thin films prepared by evaporation is of fundamental interest and has been investigated continuously for almost twenty years. Unfortunately, evaporation affords little control of structure on the nanometer scale. Controlled enlargement of a two-dimensional (2-D) array of single-sized Au nanoparticles leads to well-defined 2-D conductors. (iii) Finally, solution fabrication of thin Au films may be well-suited for surface plasmon resonance (SPR). Detection of biomolecular complex formation and/or dissociation using SPR is becoming common. The phenomenon is based on changes in reflectivity of  $\approx 50$  nm diameter Au films coated with 200-nm thick films of carboxylated dextrans.

CONTROLLED FORMATION OF CONDUCTIVE AU FILMS BY SEEDING OF  
COLLOIDAL AU NANOPARTICLE SOLUTIONS  
Bulk Optical and Electrical Properties

Based on the results of seeding of colloidal Au nanoparticles with  $\text{Au}^{3+}/\text{NH}_2\text{OH}$  in solution, it was anticipated that enlargement of surface-confined particles would proceed as shown in Figure X. Starting with a Au colloid monolayer with  $\approx 20\%$  of close-packing coverage, immersion into the seeding solution leads to particle growth. It was expected that the particles will not move (a consequence of several hundred bonds between colloidal Au surface and either  $-\text{NH}_2$  or  $-\text{SH}$  groups on the organosilane), and that (at least at early stages of growth), the particles would retain their spherical character.

Figure 13 shows visible optical spectra over time for a 12-nm Au colloid monolayer on APTMS-coated glass substrate upon immersion in a solution of 0.01 %  $\text{HAuCl}_4/4 \text{ mM NH}_2\text{OH}$ . Every ten seconds for the first minute (top panel), the absorbance continually increases from the initial colloidal Au monolayer (a). In this time frame there is a noticeable increase in total absorbance but the spectral peak near 520 nm is still clearly defined, albeit slightly red-shifted. As previously discussed, the increased extinction and the shift of  $\lambda_{\text{max}}$  to longer wavelengths are both consistent with increased dimensions for the particles being interrogated. As time progresses towards 45 minutes of immersion (bottom panel), extinction of light is large over the entire visible spectrum, including at 526 nm, the position of  $\lambda_{\text{max}}$  for the monolayer. At longer times, the absorption band broadens considerably and  $\lambda_{\text{max}}$  gradually shifts past 600 nm.

The increase in absorbance accompanying deposition of  $\text{Au}^0$  onto immobilized colloidal particles extends well into the infrared region of the spectrum. The top panel of Figure 14 shows representative optical spectra from two sets ["high" coverage (a) and "low" coverage (b)] of twenty Au colloid monolayers each from which thin Au films were grown by  $\text{Au}^{3+}/\text{NH}_2\text{OH}$  seeding. The middle and bottom panels show near-infrared absorbance over time for Au films grown from colloidal Au monolayers with high and low coverages, respectively. As expected, the absorbance of the low coverage films lags behind that of the high coverage. For example, after 9 minutes of seeding, the low-coverage sample had an absorbance about 20-25% lower than high-coverage sample exhibited after 8 minutes.

Although these surfaces comprise only a single layer of particles, as opposed to the numerous strata of spacer-linked colloidal Au in multilayers, they nevertheless exhibit similar near-IR optical spectra. In both cases, increased quantities of Au immobilization lead to decreased transmission and to a loss of wavelength sensitivity. These properties have been observed in percolating Au films prepared by evaporation, with one significant difference: in

the latter, the percolation threshold (i.e. the inflection point in insulator-conductor transition) is denoted by the point at which the absorbance becomes wavelength-independent. Here, well before the plots of near-IR absorbance vs. wavelength become horizontal, the Au films are very highly conductive; however, evaporated Au films and high-coverage  $\text{NH}_2\text{OH}$ -seeded films do share the attribute of increased absorbance at increasing wavelengths (i.e., an upward-sloping line) in the fully metallic regime. Table 3 lists resistance measurements for enlarged low-coverage and high-coverage Au colloid monolayers.

It is clear that bulk properties are reached more rapidly from high coverage surfaces. For example, after six minutes, the resistance of the high-coverage seeded surface is 1/40,000th that of the low-coverage seeded surface ( $14\ \Omega$  vs.  $650,000\ \Omega$ ). Conversion of measured resistances into resistivities by accounting for measurement geometry) indicates that both seeded films ultimately achieve extraordinarily high conductivities; for low-coverage colloidal Au monolayers immersed in seeding solution for 30 minutes, the resistivity  $\rho = 1.0 \times 10^{-5}\ \Omega\text{-cm}$ , in comparison with  $2.44 \times 10^{-6}\ \Omega\text{-cm}$  for pure Au at room temperature. Thus, these films are within a factor of four of the conductivity of pure Au (of the same thickness), and far exceed the conductivities for a variety of other metals.

Given the high conductivity of these films, they can be used as working electrodes in cyclic voltammetry (CV) experiments, see Figure 15. The top panel shows cyclic voltammograms for  $[\text{Ru}(\text{NH}_3)_6]^{3+}$  at three different scan rates for a high-coverage, 17-minute seeded Au film. Quasi-reversible voltammetry is obtained, with an  $E^\circ$  of  $-0.23\ \text{V}$  vs. SCE, and peak-to-peak separations ( $\Delta E_p$ ) of  $135\ \text{mV}$  at  $50\ \text{mV/s}$ ,  $180\ \text{mV}$  at  $100\ \text{mV/s}$ , and  $210\ \text{mV}$  at  $200\ \text{mV/s}$ . The increase in  $\Delta E_p$  with increasing scan rate is indicative of one (or more) barriers to heterogeneous electron transfer (ET), among which could include lack of cleanliness of the electrode, poor ET kinetics at films deposited from solution, or barriers due to complex morphology (vide infra). In any case, there is a clear difference between the highly conductive and partially conductive films (bottom panel): the CV for the Au colloid monolayer immersed for three minutes in to  $0.01\%\ \text{HAuCl}_4/0.4\ \text{mM}\ \text{NH}_2\text{OH}$ , the magnitude of the cathodic current is roughly ten-fold smaller than for the highly conductive films; the broad, drawn-out nature of the CV results in large part from the IR drop across the electrode.

The third set of resistance measurements in Table 3 were made on Au colloid multilayers exposed to  $0.01\%\ \text{HAuCl}_4/0.4\ \text{mM}\ \text{NH}_2\text{OH}$  for varying lengths of time. From the resistance data and UV-Vis-near IR spectra, it appears that catalysis of the  $\text{Au}^{3+} \rightarrow \text{Au}^0$

reaction is not facile on colloidal Au particles (at least partially) coated with organic adsorbates such as 2-mercaptoethylamine. Even though the initial, four-layer sample had an absorbance of  $\approx 0.4$  (i.e. four times as many particles), the sample resistance is higher per unit time than for the high-coverage Au colloid monolayer. Moreover, although the resistance drops by five orders of magnitude, the near-IR absorbance does not become completely wavelength-independent after 10 minutes of seeding.

Despite these differences, however, the three types of samples discussed in Table 3, namely high- and low-coverage Au colloid monolayers and Au colloid multilayers, all comprise good substrates for  $\text{Au}^{3+}/\text{NH}_2\text{OH}$  seeding: all exhibit precipitous decreases in resistance, and all take on bulk optical properties in the near-IR similar to those exhibited by evaporated Au films.

#### Film Nanostructure by AFM and FE-SEM

While the bulk measurements described above certainly provide evidence that immobilized Au nanoparticles can be enlarged by  $\text{Au}^{3+}/\text{NH}_2\text{OH}$  seeding, they do not provide the information on particle size and shape. Likewise, while near-IR and resistance data clearly established differences in the approach to metallic behavior for Au colloid monolayers with high and low particle coverages, they do not yield any insight into the actual mechanism of particle coalescence. Both these issues can be resolved by a combination of AFM and FE-SEM analysis. Both types of measurements are essential, since only FE-SEM reveals the true particle positions and dimensions in the x-y plane, and only AFM can measure film thicknesses in the z-direction.

The time course of  $\text{Au}^{3+}/\text{NH}_2\text{OH}$ -mediated enlargement of immobilized Au nanoparticles at low coverage and at high coverage are revealed by AFM images in Figures 10 and 11, respectively. Each figure is made up of six images, starting with the monolayer (A), and follows the evolution of highly conductive films over the last five images (B-F). For each, the latter five images were acquired from the same samples from which resistance data were obtained (Table 3).

The AFM image of the low-coverage Au colloid monolayer (Figure 10, panel A) shows individual particles between 12 and 15 nm in height and with flat spaces in between. The corresponding panel in Figure 11 shows a close-packed arrangement of particles. This is an artifact of AFM tip convolution on these samples – previous FE-SEM and TEM data have

conclusively shown that images such as these correspond to 0.2-0.3 monolayers. Nevertheless, the two images provide a clear view of the differences in initial particle coverage.

For the low-coverage film,  $\text{Au}^{3+}/\text{NH}_2\text{OH}$  seeding leads to evolution of features that are both taller and broader. The line scan corresponding to Panel F in Figure 10 shows features as tall as 50 nm and as wide as 75 nm (the line scan indicates a width of  $\approx 150$  nm, but true particle dimensions in the x-y plane are actually only about half those recorded. Moreover, the features are substantially closer together than the original features imaged on the colloidal monolayer. Because of AFM tip convolution, it is impossible to determine interparticle spacing, but it is worth noting that the samples corresponding to images D, E, and certainly F conduct electricity (Table 3). Therefore, there are extensive domains where particles are in contact or are close enough to each other to allow efficient electron tunneling. AFM tip convolution also prevents calculation of the particle ellipticity G, but there appear to be none of the high-aspect ratio rod-shaped particles synthesized during  $\text{Au}^{3+}/\text{NH}_2\text{OH}$  seeding in solution.

$\text{Au}^{3+}/\text{NH}_2\text{OH}$  seeding on the high-coverage Au colloid monolayer (Figure 11) follows a different pattern than that described for the low-coverage sample (Figure 10). While comparison of Panels A and F clearly indicate an increase in both particle height and width, neither is as dramatic as seen for the low-coverage film. For example, the largest features for the sample imaged in Figure 11, Panel F (high coverage, 17 min.-seeding) (or any other image of the same surface) is  $\approx 25$  nm, compared to  $\approx 50$  nm for the sample imaged in Figure 10, Panel F (low coverage, 30 min.-seeding) (or any other image of the same surface). At earlier times, the high coverage surface appears even flatter: the most prominent vertical features in line scans of Panels B, C, and D of Figure 11 are less than 18 nm high.

Short-time seeding of low-coverage Au colloid monolayers leads to a startlingly different (but expected) nanostructure (Figure 12, panel B): after 6 minutes, there is little particle fusion. To the contrary, a collection of isolated larger particles is seen, many of which are elliptically shaped. Also, about 10-15% of the particles are isolated spheres of 40-50 nm diameter. Clearly, increasing the interparticle spacing promotes "solution-like" enlargement, and notwithstanding the fused particles, the resulting surface looks like one that might be obtained by self-assembly of a 50-nm diameter colloidal Au particles prepared by the Frens method.

FE-SEM images of Au films derived from prolonged  $\text{Au}^{3+}/\text{NH}_2\text{OH}$  seeding of high-coverage and low-coverage Au colloid monolayers (panels **C** and **D**, respectively, of Figure 12) are far more similar than their predecessors. Both films exhibit large-scale particle fusion, with all vestiges of the original nanostructure completely obscured. The only discernable difference between the samples is the presence of scattered "holes" in the low-coverage film, likely a product of incomplete coalescence of large particles.

The images in Figures 10-12 reveal how two very different growth mechanisms can yield equally conductive surfaces by  $\text{Au}^{3+}/\text{NH}_2\text{OH}$  seeding: at high coverages, early-time coalescence of smaller particles leads to a granular film, while at low coverage, isolated particles are seeded to form distinct, larger particles prior to their ultimate fusion.

#### Nanometer-Scale Optical Properties

The low transmittance of metallic Au/air interface in the near-IR is an intrinsic optical property of Au that depends solely on its wavelength-dependent dielectric properties. In contrast, several optical properties of Au depend on nanostructure, including SERS, SPR, and non-linear optical behavior. Accordingly, we sought to investigate the effects of particle enlargement and surface roughening via  $\text{Au}^{3+}/\text{NH}_2\text{OH}$  seeding on these optical phenomena.

Figure 13 shows SERS spectra for 10 mM solutions of BPE drop-coated onto a 12-nm diameter colloidal Au/APTMS/glass substrate (a) and onto identical substrates after immersion in 0.01 %  $\text{HAuCl}_4/0.4$  mM  $\text{NH}_2\text{OH}$  for 1 (b), 6 (c) and 17 minutes (d). Seeding leads to significant increases in signal ( $\approx 50$ ) compared to the relatively weakly enhancing Au colloid monolayer. These surfaces give SERS enhancements equivalent to surfaces prepared by more effort-intensive (and expensive) methods as evaporation or sputtering.

While SERS is extraordinarily sensitive to nanostructure at the surfaces of free electron metals like Au, it is a rather poor probe of interior nanostructure, as long as it does not impact bulk optical properties. In contrast, SPR depends on propagation of surface plasmons through thin Au films on glass substrates under conditions of total internal reflection. Since the plasmons are launched by evanescent waves that penetrate the Au to a depth of  $\approx 150$  nm, internal film structure is critical.

Figure 14 shows the variety of SPR responses that can be obtained with evaporated and colloidal Au films. The top panel shows simulated reflectance vs. excitation angle curves for a 50-nm thick evaporated Au film, and experimental data for a 12-nm diameter colloidal Au/APTMS/glass surface and an eight-layer 12-nm diameter Au colloid multilayer. While

the evaporated films shows a sharp minimum in reflectivity that comprises the basis for biological applications of SPR, both the Au colloid monolayer and multilayer exhibit broad reflectivity profiles. For the monolayer, the high reflectivity is due to the low sample absorbance at 632.8 nm; the large extinction of the multilayer at this wavelength leads to low reflectivity.

Particle enlargement and/or coalescence by  $\text{NH}_2\text{OH}$  seeding leads to increased definition in SPR reflectivity curves for low- and high-coverage Au colloid monolayers (middle panel) as well as for Au colloid multilayers (bottom panel). For the latter, after a 10-minute immersion in the seeding bath, there is a further decrease in reflectivity, with concomitant evolution of fine structure. In particular, there is a spike at  $\approx 41^\circ$ , and a sinusoidal variation in reflectivity from  $45^\circ$  to  $65^\circ$ . Changes in reflectivity at the former (the critical angle) are expected; the origin of the latter feature clearly results from changes in film morphology.

Of greater interest are the changes in the monolayer reflectivity after a 10-minute immersion in  $\text{Au}^{3+}/\text{NH}_2\text{OH}$ . For the high-coverage surface, there is now a broad minimum in reflectivity that only slowly dissipates over  $20^\circ$ . The low-coverage surface shares a similar profile, but minimum is less shallow. This difference is magnified at 20- and 30-minute immersion times. In general, there is an increase in reflectivity, as expected with 632-nm excitation for Au films that are greater than 50 nm thick. More importantly, while the minimum in reflectivity for the high coverage film is only slightly more pronounced than for a 10-minute immersion, a clean, relatively narrow minimum has evolved on the low-coverage surface. It is surprising that the SPR signature is so dramatically distinct for two films that have the same conductivity (Table 3), the same optical spectrum (Figure 14), and an almost identical nanostructure (panels C and D of Figure 12); at the same time, though, it is reasonable to expect that the SPR response, which is ideal for a 50-nm thick Au film with 3-4 nm roughness, would be better on the low-coverage film, in which particle growth proceeded prior to roughly 40-45 nm in diameter prior to coalescence.  $\text{Au}^{3+}/\text{NH}_2\text{OH}$  seeding of Au colloid monolayers with even lower coverages would lead to sharper SPR curves, via growth of isolated particles to even larger dimensions before fusion.

$\text{Au}^{3+}/\text{NH}_2\text{OH}$  seeding of colloidal Au films provides entry to a series of complex Au nanostructures that have been probed by UV-Vis near-IR, electrochemistry, resistance measurements, atomic absorption, AFM, FE-SEM, SERS, and SPR. For colloidal Au

multilayers linked by 2-mercaptoethylamine, particle enlargement proceeds with the expected consequences, namely increased UV-Vis near-IR extinction, and decreased in resistance and reflectivity. The behavior of Au colloid monolayers depends markedly on particle coverage. At high coverage, seeding leads to early particle coalescence, resulting in films

5 indistinguishable from those prepared by evaporation of Au onto thiol-terminated glass substrates (which is widely used to promote Au adhesion). Indeed, seeding of high-coverage Au colloid monolayers can be considered a vacuum-free route to production of thin films remarkably similar to those produced by evaporation. At low coverage, the isolated particles grow individually into spheres, rods, and ellipses, in analogy to the process in solution.  
10 Continued growth leads to conductive films whose reflectivity vs. excitation-angle curves exhibits pronounced minima. Once again, this property resembles that of evaporated Au films of narrowly-defined specifications that are used for SPR experiments.

Methodology to generate films composed of metal nanoparticles assembled in a stepwise fashion entirely from solution is presented; thus, there are few constraints on  
15 substrate size or shape. By controlling feature size, spacing, shape, and composition, optical and electrical properties may be tuned. Films assembled using crosslinker,  $\leq 8\text{\AA}$  in length have optical properties and conductivity comparable to their bulk metal counterpart. These were shown to be suitable for use as planar electrodes or SERS substrates. Au volume fractions were shown to be constant at all film heights, close to the critical volume fraction  
20 predicted by scaling law for the metal-insulator transition. EFM reveals the presence of conductive and insulating regions consistent with the metal-insulator transition. Film roughness is believed to be responsible for the broad SPR curve observed from multilayer films on Au and glass and contribute to the SERS enhancement for BPE absorbed at Au or Ag nanoparticle assemblies. The fabrication of patterned multilayers with a low error density  
25 using microcontact printing and construction of biologically active HRP-linked multilayers provide the groundwork for the development of colloidal nanoparticle devices as biosensor and electronics.

## 30 MANUFACTURE AND CHARACTERIZATION OF COLLOIDAL AU AND AG MULTILAYERS

The present invention is also directed to the manufacture of colloidal metal monolayers, particularly Au and Ag multilayers.



### Sample Fabrication and Characterization

Multilayer films are generated in a stepwise process from Au or Ag hydrosols as follows. A monolayer of Au or Ag colloid on a silanized SiO<sub>2</sub> substrate (APTMS, MPTMS, MPMDMS) is briefly immersed in a dilute solution (5 mM, 10 min) of bifunctional crosslinker, scrupulously rinsed, and immersed in Au or Ag solutions (40-60 min), where additional particle binding occurs. Multilayer films result from repetitive exposure to crosslinker and sol. The inherent flexibility of the stepwise assembly process provides a platform for assembly of any combination of nanoparticles. In general, almost arbitrarily thick films of any size Ag or Au nanoparticle can be made using this protocol, although derivatization times depend on particle concentration and size.

Photographs of multilayers assembled from Au and Ag metal nanoparticles show an increase in particle coverage as the number of layers increase. Films assembled from 11-nm diameter Au nanoparticles linked by MEA initially change color from pink to blue; after 15 exposures to MEA/Au colloid have a final appearance similar in color and reflectivity to bulk Au, suggestive of bulk metal behavior. Comparable color shifts from yellow to green are observed with films composed of polydispersed MEA-linked Ag nanoparticles and at higher coverage, a bulk Ag appearance is observed. Composite films of alternating layers of colloidal Ag and Au undergo a similar color shift. Interestingly, a large portion of the visible spectrum is traversed by mixing just two types of particles. Such films might have applications as dichroic coatings. Figure 15 shows the optical absorbance spectra of such Ag/Au colloid multilayers both in H<sub>2</sub>O (top) and in air (bottom). The spectra in H<sub>2</sub>O are interesting in that they comprise the surface plasmon band of both Au colloid ( $\lambda_{\text{max}}=518$  nm) and Ag colloid ( $\lambda_{\text{max}}=408$  nm). Deposition of a layer of nanoparticle results in an increase at the respective  $\lambda_{\text{max}}$ . For example, the change in absorbance from 0.41 (top panel, curve b) to 0.60 (top panel, curve c) at  $\lambda_{\text{max}}=408$  nm indicates the addition of a layer of Ag particles. Notice only negligible change in absorbance occurs at  $\lambda_{\text{max}}=518$  nm. A similar observation can be made for the addition of an Au colloid layer (e.g. spectra d and e, top panel). Upon drying of the film, aggregation of the particles is indicated by a red shift in the  $\lambda_{\text{max}}$  and a broadening of the spectra. Information about the composition of the film is lost due to the combination of individual plasmon bands into collective plasmon oscillations (bottom panel). Likewise, optical spectra of Au and Ag colloidal multilayers display an increase in

absorbance over the entire visible region (350 - 820 nm) corresponding to additional particle coverage with each crosslinker/colloid.

To develop functional nanostructured arrays with tailored properties, the ability to predetermine the nanoparticle coverage is essential. To gain a more accurate view of the surface architecture, detailed analysis of film morphology was carried out using AFM and FE-SEM. These data indicate a porous, networked structure. AFM images acquired on 2-mercaptoethanol-linked colloidal Au multilayer as a function of the number of Au colloid layers reveal small segregated areas of agglomerated colloid which evolve into connected peaks of colloidal Au. By 11 Au layers, large areas of uninterrupted colloid form a porous interconnected network suggestive of conductive pathways. The AFM line scans depict an increase in film depth after each Au colloid treatment and the peaks and valleys associated with film formation. In contrast to AFM, which depicts a more closely packed film the increased lateral resolution of FE-SEM reveals that discrete colloidal islands are present even after exposure of a Au colloid monolayer to a single additional layer of Au. Interestingly, in a high-magnification FE-SEM of Au/Ag particle composite film, the spherical monodisperse Au colloid is easily distinguished from the heterogenous Ag nanoparticles.

Even in the absence of detailed nanometer-scale images, accurate information about particle coverage can be obtained by simple uv-vis measurements on wet or dry samples. This is illustrated by the data in Figure 17, which plots absorbance vs. particle coverage as determined by atomic absorption analysis of digested surfaces. (Note that the combination of TEM, which gives very accurate particle size, and AA, which yields very accurate measurements of total Au, is an extremely trustworthy approach to ascertain total particle coverage, provided the particles are monodisperse). These data are noteworthy in several respects. (i) Good linearity is found both for wet and dried samples, even though the optical spectra of the dried samples is red-shifted and broadened. (ii) A previously published plot of particle coverage vs. number of exposures was also linear, indicating that the same number particles were immobilized in each treatment, despite what should in theory be an increase in surface roughness and in available surface area with each successive layer. These data are re-confirmed via a linear plot of average film height vs. number of layers. The point is that both past and present data show that the same numbers of particles are immobilized with each treatment. The data in Figure 17 indicate that each particle contributes the same amount of extinction irrespective of its position in the film. This means that Beer's Law is as powerful as TEM/AA or FE-SEM or AFM for quantitation of particle coverage in this regime.

Moreover, the result attests to the non-ordered arrangement of particles: if the particles studies were positioned directly atop one another to form columns perpendicular to the substrate plane (i.e., parallel to the propagation direction of the electric field vector), Beer's Law would not be obeyed.

5       Molecules with two or more functional groups capable of strong interactions with metallic Au can be used to crosslink colloidal Au particles. Table 4 lists potential crosslinkers. Functional groups used include but are not limited to thiol, amine, siloxane, alcohol and isocyanide. Binding of the latter functional group to Au has been studied in detail by Ontko & Angelici, *Langmuir* 1998, 14:1684-1691. Henderson, et al., *Inorg. Chim.*  
10 *Acta* 1996, 242:115-125, have previously described the binding of -NC terminated phenylenes to Au clusters. Likewise, thiol Au chemistry has been extensively probed with respect to self-assembled monolayer formation, and the synthesis of thiol capped Au nanoparticles, have extended characterization to Au nanoclusters. Amine groups such as those on MEA or APTMS have previously been shown to electrostatically couple Au  
15 particles. Indeed, low concentrations of each crosslinker added to a solution of colloidal Au cause flocculation.

Proteins can also be used to connect layers of Au nanoparticles. Interest in such biomolecule-metal hybrid films derives from the ability to couple biomolecules to Au colloids without appreciable loss of native biological activity. Applications for these systems  
20 include biosensors, electrochemical analysis, and biocompatible coatings. Figure 18 shows optical spectra for 11-nm diameter Au colloid multilayers fabricated with HRP as a crosslinker between each layer. As with other crosslinkers, a relatively linear change in absorbance at  $\lambda_{\max}$  is observed with each colloid treatment. The inset to Figure 18 is a graph of the HRP activity as a function of the number of Au colloid layers. For these films a  
25 decrease in activity is observed with each colloid exposure, but the activity level returns after the next HRP treatment. The ability to preserve activity in multilayers with smaller particles is significant, and has previously been observed in less-well-defined assemblies.

The mechanism of colloid addition appears to be independent of crosslinker type, with all films displaying an increase in absorbance with each additional layer of colloid.  
30 However, bulk optical properties are dramatically affected by choice of crosslinker as seen by Uv-Vis/NIR transmission spectra of Au colloid multilayer films prepared using three bifunctional crosslinkers [MEA (top), APTMS (middle), and 1,6-hexanedithiol (bottom)], as

a function of number of particle and crosslinker treatments. With MEA-linked films, a decrease in transmission is seen from  $\geq 90\%$  between 800 and 2500 nm to  $\leq 15\%$  with nine layers of particle. The high degree of reflectivity over a broad wavelength range is typical of metallic behavior. Colloidal Au multilayers comprised of nine or more layers appear to the eye indistinguishable from evaporated Au films and have a Uv-Vis/NIR spectra comparable to evaporated metal films and films generated by reduction of  $\text{Au}^{3+}$  onto an Au colloid monolayer. This suggests similarities between films of closely packed Au nanoparticles and bulk Au films. Moreover, colloid linked multilayer films, Au plated films, and evaporated Au films turn from blue to a metallic gold luster as the Au coverage is increased. That 2-mercaptoethanol-linked multilayer films also undergo the same large decrease in %T as in evaporated metal films was reported by Musick, et al., *Chem. Mater.* 1997, 9:1499-1502.

The transmission in the NIR region is nearly wavelength independent for 2-mercaptoethanol- and MEA-linked Au colloid multilayers. In contrast, films generated from longer crosslinking molecules (APTMS, 1,6-hexanedithiol, and diisocyanides) exhibit markedly different optical properties. With APTMS-linked Au colloid multilayers, the transmittance in the visible decreases linearly as a function of colloid coverage, as with MEA. However, the NIR region remains relatively transparent, and wavelength dependent. Similar results are obtained with 1, 6-hexanedithiol-linked films. Comparison of the optical spectra with molecular structures in demonstrates that films assembled from shorter crosslinkers resemble bulk Au, suggesting that a collective particle mode contributes to the NIR absorption behavior. Interestingly, a difference of only  $\approx 1.5 \text{ \AA}$  in molecular length results in significant differences in optical properties. A series of aryl diisocyanides were synthesized for a controlled study of crosslinker length (Table 4) versus optical properties (Figure 19). Despite a  $7 \text{ \AA}$  difference in crosslinker length between 1, 2, and 3, the optical properties in the visible region 400-800 nm are nearly indistinguishable. After greater than 20 crosslinker/Au colloid treatments (11-nm diameter), films are less than 5% transmissive at 600 nm and to the eye appear dark blue. Films prepared from 1 display strong wavelength dependence in the near IR, similar to APTMS-linked films of comparable coverage. It is interesting to note that the predicted difference in length for these two molecules is  $\leq 1 \text{ \AA}$ . Films prepared using 2 and 3 also have a wavelength-dependent transmission, but it is less pronounced; moreover, the films are more transmissive. Thus, at 1500 nm, with 20+ layers, films made using 1 are 40% transmissive, while those of 2 and 3 are 60% transmissive.

The data in Figures 18 and 19 suggest that the optical properties of colloidal metal nanoparticles are described by four distinct ranges determined by the interparticle spacing of the Au nanoparticles. (i) Colloid films fabricated from crosslinkers with a molecular length (ML)  $\leq 8$  Å display properties much like their bulk metal counterparts: a broad surface plasmon band, wavelength independence from 800 to 2500 nm, and a linear decrease in transmission from 350 to 2500 nm with each colloid treatment. (ii) For films where crosslinker ML is  $8 < ML < 12$  Å, intermediate behavior is observed; a decrease in transmission is observed with the addition of Au colloid from 300 to 800 nm, the particle plasmon band is visible even at high coverage, and there is a moderate wavelength dependence observed between 800 and 2500 nm. Contrary to this behavior, the transmission spectra of films generated from 1,6-hexanedithiol and Au colloid have properties that resemble films assembled from shorter crosslinkers [i.e., APTMS or 1]. This suggests the possibility that to both ends of the dithiol may be bound to the same particle, thereby allowing two colloids to approach each other closer than predicted. (iii) For films with crosslinker ML  $> 12$  Å the visible region is identical, between 700 and 1000 nm a strong wavelength dependence is observed, and from 1000 to 2500 nm the films are transparent with no observed wavelength dependence, even with as many as 25 treatments of crosslinker and colloid. Finally, (iv) when the crosslinker dimensions are of the same order of magnitude as the particles, i.e., multiple nanometers (as in BSA and HRP), there is no interaction between particles, and the multilayers remain essentially transparent in the near IR. The ability to precisely tune optical properties for an arbitrary thickness differentiates Au colloid multilayers from evaporated films, where, for a given thickness, the optical properties are relatively fixed.

Both the dimension of the spacer and the way multilayers are prepared impact the film's volume fraction of metal. Figure 20 is a plot of volume fraction of Au ( $V_{Au}$ ) versus treatments of Au colloid and MEA. Several methods of calculating  $V_{Au}$  will be discussed. Importantly, the precise volume fraction depends on the method of calculation. Note, however, that  $V_{Au}$  remains essentially unchanged with each colloid treatment (for each method of calculation). Determining  $V_{Au}$  from only AFM data, film volume and maximum ( $\square$ ) and average ( $\square$ ) film heights results in  $V_{Au}$  of  $0.5 \pm 0.02$  and  $0.1 \pm 0.03$ , respectively. An  $V_{Au}=0.5$  is obtained from the film volume calculated by integrating the area under the peaks at the maximum film depth in an AFM. From a random sequential absorption model,

the maximum packing for hard spheres results in a volume fraction of approximately 0.5. However, this is the maximum possible volume fraction since the AFM is incapable of delineating volume under a feature. For example, a stack of spheres is viewed as a domed cylinder despite a significant contribution to the total film volume from void volume. Other attributes of the multilayer system should cause substantial deviation from this model as well. For example, initial colloid placement is not random. Colloids have a negative charge and deposit with an average interparticle spacing that is smaller than predicted by random sequential absorption. Likewise, most crosslinkers are selective only for metal. Therefore, the deposition of additional layers is confined to regions previously occupied by colloid. Thus, a decrease in predicted  $V_{Au}$  is expected. Similarly, a  $V_{Au} = 0.1$  is below the volume fraction predicted for a 2-D or 3-D array of conductors (equal to 0.5 and 0.3, respectively), yet these films can be remarkably conductive (see below). When particle size and coverage are determined by TEM and atomic absorption spectrometry, intermediate volume fractions are found. Total Au volume is found by AA and from the volume occupied by each nanoparticle the number of particles per unit area is determined. Considering the total volume occupied by Au and the total volume from the size and maximum height of the AFM scan area a  $V_{Au} = 0.21 \pm 0.04$  ( $\square$ ) is found. This is in good agreement with the volume fraction determined from the diameter of the particle and the coverage ( $\square$ ) of  $V_{Au} = 0.23 \pm 0.04$ . This method assumes that film height is increased only by one colloid diameter per treatment and uses the coverage information to determine the amount of colloid deposited. These are felt to be the best measures of volume fraction. Due to the mountain-like nature of the films,  $V_{Au}$  is extremely dependent upon the depth with the possibility of a higher  $V_{Au}$  in the lower layers. The important point from these calculations is that, irrespective of the method used, these are not significant changes in volume fraction during growth.

Electrical properties of discontinuous metal films and mixed metal particle composites have been demonstrated to depend on the volume fraction of metal. Scaling law predicts a dimensionality-dependent critical point,  $p_c$ , where at the metal-insulator transition  $p_c = V_{Au}$ . For a 2-D case,  $p_c$  equals 0.5 and is between 0.25 and 0.31 for a 3-D system. These values have been explored experimentally numerous times simple systems, such as discontinuous metal films, coevaporated materials, or physical mixtures of carbon and teflon particles. Figure 21 is a log plot of film resistance versus number of Au colloid exposures for 2-mercaptoethylamine, 1,6-hexanedithiol, and 2-mercaptoethanol linked films. The sharp

decrease in resistance observed for each crosslinker after 5 to 6 exposures to Au colloid can be attributed to a change in dimensionality (2-D to 3-D). For 2-mercaptoethanol linked films, the most conductive final resistance ( $70\ \Omega$ ) is reached after 10 layers of Au colloid. This corresponds to a resistivity equal to  $2 \times 10^{-4}\ \Omega\text{-cm}$ , approximately 200 times lower than bulk Au. As described above  $V_{Au}$  is constant (see Figure 20) and approximately 0.23 for all Au coverages (11-nm diameter) in reasonable agreement with the predicted  $V_{Au}$  of 0.25 for a 3-D system. Gadenne, et al., *Thins Solid Films* 1992, 221:183-190, noted similar behavior in Au/ $\text{Al}_2\text{O}_3$  composite films, where a critical film height indicated the onset of conductivity; however, germane to conductivity measurements is a second explanation in which a change in local volume fraction due to heterogeneity in the conductor dispersion results in planes of varying volume fraction. Such an explanation was offered to explain anomalous optical absorbance of Au particle/ $\text{SiO}_2$  dispersions and may apply to the morphology of Au colloid multilayers. In comparison to conductive films crosslinked by MEA or 2-mercaptoethanol, films of 1,6-hexanedithiol- a longer crosslinker- reach a minimum resistance of  $1\ \text{M}\Omega$ . Similar behavior is observed for multilayers linked by the diisocyanophenylene's 1, 2, and 3, displayed in Figure 22. Once again, a decrease in resistance occurs after the addition of 4 to 5 layers of colloid, but the final minimum resistances for crosslinkers 1, 2, and 3 are 5, 18, and  $35\ \text{M}\Omega$ , respectively –  $10^5$  larger as for shorter crosslinkers. Here a correlation is observed between the minimum resistance and the length of the molecule; in this sense, DC resistance is comparable to the optical properties. Similar systems consisting of thiol coated Au nanoparticles (<5-nm diameter) have been examined by the Murray group, but no systematic examination of chain length or particle size vs. conductivity was reported.

#### Applications of Au Colloid Multilayers

The ability to generate conductive films from inexpensive solutions of metal nanoparticles offers applications in device fabrication, particularly on rough or sensitive substrates. In patterned multilayer surfaces made by microcontact printing, a polymeric negative of an object is constructed by polymerization of a polydimethylsiloxane (PDMS) solution containing the master (a grating with a  $3\ \mu\text{m}$  period). After hardening, the object is removed and an imprint remains in the polymer. In the PDMS negative was "inked" with  $\text{HOOC}(\text{CH}_2)_{15}\text{SH}$ , a molecule with a relatively low affinity for colloidal Au. The surface was then treated with MEA to fill in the interstices and subsequently exposed to a solution of

11-nm diameter Au colloid. The pattern was developed further with two additional exposures to MEA and Au colloid. A replica of the original grating surface can be seen in each image. Some nonspecific colloid binding is observed between the lines; clearly there is some binding of Au to carboxylate. Nonetheless, the images show that multilayers of 12-nm diameter colloidal metal particles can be formed on patterned surfaces.

Once they are metallic, Au multilayers can be used in lieu of evaporated metal films for a variety of surface chemical applications. For example, the cyclic voltammetric behavior of Au colloid films has been examined as a function of number of layers of colloidal Au. For samples on glass prepared with MEA as a crosslinker, films comprising less than 10 layers have poorly defined voltammetry due to the high resistance of the electrodes. At  $\geq 10$  layers of Au nanoparticles typical diffusion limited voltammetry (comparable to a planar electrode) is observed. The peak potential difference ( $\Delta E_p$ ) decreases with increasing numbers of colloidal layers. For example, an observed  $\Delta E_p$  for a 10 layer electrode is 114 mV but is reduced to 82 mV for the 15 layer electrode. Even with  $\Delta E_p = 114$  mV, these still comprise excellent examples of electrodes self-assembled directly from solution. Cyclic voltammetry of  $\text{KFe}(\text{CN})_6$  in 0.1 M  $\text{Na}_2\text{SO}_4$  was also investigated for Au colloid multilayers assembled on In-doped  $\text{SnO}_2$ . Here, a decrease in  $\Delta E_p$  was also observed for increasing numbers of colloidal Au treatments. In this case, the transparent underlayer is conductive with an  $R \approx 70 \Omega\text{-cm}$ ; additional layers of Au likely reduce the resistance and increase the active area, but most importantly, improve the kinetics for heterogenous electron transfer.

Au colloid multilayers can also be used for surface plasmon resonance (SPR) and surface enhanced Raman scattering (SERS), surface spectroscopies traditionally carried out with continuous Au films. Figure 23 shows SPR scans of a bare Au film (39 nm thick) and after 1, 2, and 3 exposures to MEA/11-nm diameter colloidal Au. After one treatment of Au colloid, a decrease in percent reflectivity, a  $1.4^\circ$  shift in plasmon minimum, and an overall broadening of the curve are observed. A 5-nm thick film of organic or protein molecules would result in only a  $0.2^\circ$  shift in reflectivity with no band broadening or change in percent reflectivity. The Fresnel equations assume a homogenous dielectric constant of the absorbed layers and do not include scattering or absorption processes by metal nanoparticles. Furthermore, individual metal nanoparticles can support plasmon propagation at critical wave lengths. These effects are believed to contribute significantly to the perturbations in the SPR curves, particularly the possibility that individual Au colloids may act as nanoscale roughness



features. Previously, similar results were obtained for Ag films with 50, 100, and 200 nm underlayers of CaF<sub>2</sub>: the surface roughness of CaF<sub>2</sub> increases with thickness. Related experiments were conducted with LiF and an Au overlayer. Also note that enhanced scattering and light emission have both been noted for roughened films of Au and Ag.

5 Multilayers assembled directly onto functionalized glass (i.e., with no Au film) substrates display a broad reflectivity band as a function of angle with 632.8-nm irradiation even after 13 treatments of colloid. Interestingly these films are highly conductive and appear like bulk Au to the eye. However, when examined by SPR, a minimum in the reflectance curve is apparent with the first two treatments, but disappears at successive  
10 treatments. This contrasts with bulk Au which, at a critical thickness, displays a sharp minimum in percent reflectance. A minimum percent reflectance is observed after 6 treatments. Increasing Au colloid treatment results in a flat featureless spectrum with  $\approx 20\%$  reflectance. Very similar curves were obtained for 526.8-nm excitation.

The roughness associated with the colloid multilayer film is useful for surface  
15 enhanced Raman scattering (SERS). Typical substrates include aggregated metal nanoparticle clusters, electrochemically roughened Ag films, and colloid monolayers. The film nanostructure has a profound effect on the observed enhancement. In this regard, Baker, et al., *J. Phys. Chem. B* 1998, 102:9404-9413, have reported combinatorially-designed SERS substrates fabricated by electroless deposition of Ag onto Au colloid arrays. Figure 24 shows  
20 a SERS spectra for BPE absorbed on an Ag nanoparticle 2-mercaptoethanol linked multilayer. The spectra for 10 mM BPE solution with 647.1 nm excitation is featureless (A), and for an as-prepared multilayer, two weak peaks at 1605 and 1645 cm<sup>-1</sup> are visible (B). Interestingly, after exposure to UV radiation for 5 minutes prior to BPE exposure there is a substantial increase in the observed SERS spectra (D). This suggests that 2-mercaptoethanol  
25 rearranges to coat the top most portion of the Ag multilayer and could shield BPE absorption onto the surface, or that the active sites responsible for the SERS signal are not solely due to BPE confined to the top most layer of colloid. The electric field enhancement may occur between two or more colloids. Indeed, Keating, et al., *J. Phys. Chem. B* 1998, 102:9414-9425 have reported an SERS enhancement from metal nanoparticle sandwiches using  
30 cytochrome c as a probe molecule. A comparable increase in intensity was found for mixed Au and Ag nanoparticle multilayers after extended irradiation with 647.1 nm light.

Presumably, enhancement is due to the heat- or ozone- induced removal of excess 2-mercaptoethanol or rearrangement of the colloid multilayer film.

## EXAMPLES

5           General protocols for synthesis, characterization, handling, and storage of colloidal Au solutions – including for 17 nM, 12-nm diameter particles – have been previously described in Grabar, et al., *Anal. Chem.* 1995, 67:735-43; Bright, et al., *Langmuir* 1996, 12:810-17; Freeman, et al., *Science* 1995, 267:1629-32; and Grabar, et al., *Langmuir* 1996, 12:2523-61; each specifically incorporated by reference. Na<sub>3</sub>citrate, NaBH<sub>4</sub>, HCl, HNO<sub>3</sub>, NaOH, H<sub>2</sub>SO<sub>4</sub>,  
10           and aqueous H<sub>2</sub>O<sub>2</sub> were obtained from J.T. Baker, Sigma-Aldrich, Fisher (Acros), or VWR and used without further purification. 1,6-hexanedithiol, ethylenediaminetetraacetic acid dihydrate, disodium salt (EDTA), Na<sub>2</sub>SO<sub>4</sub>, trans-4,4'-bis-(4-pyridyl)ethylene (BPE), 2-mercaptoethylamine and were purchased from Aldrich. NH<sub>2</sub>OH·HCl (henceforth NH<sub>2</sub>OH) and were purchased from Acros or Aldrich. [Ru(NH<sub>3</sub>)<sub>6</sub>]Cl<sub>3</sub> was obtained from Strem  
15           Chemicals. 3-aminopropyltrimethoxysilane (APTMS) and 3-mercaptopropyltrimethoxysilane (MPTMS) were purchased from United Chemical Technologies or Aldrich. The following materials were obtained from Sigma: horseradish peroxidase, 2-mercaptoethanol, 2-mercaptoethylamine (MEA). 3-mercaptopropyltrimethoxysilane (MPTMS), and 3-mercaptopropylmethyldimethoxysilane (MPMDMS) were purchased from Gilest. H<sub>2</sub>O was  
20           purified to  $\geq 18 \Omega$  with a Bamstead Nanopure water purification system. All chemicals were used as received except for BPE, which was recrystallized several times from CH<sub>3</sub>OH/H<sub>2</sub>O. Glass substrates (microscope slides and cover slips) were obtained from VWR or Fisher Scientific Co. and cleaned using protocols previously described in Grabar, et al., *Langmuir*, 1996, 12:2353-61, prior to derivatization.

25

### EXAMPLE 1. Atomic Absorption Spectroscopy

          Samples for atomic absorption (AA) were prepared by digesting 0.1 ml of colloidal Au solution with 30  $\mu$ l of concentrated HNO<sub>3</sub> and 30  $\mu$ l of concentrated HCl, and diluted to 10 ml. 0.1 ml of this solution was mixed with 0.1 ml of 2% HNO<sub>3</sub> and 0.8 ml of H<sub>2</sub>O for  
30           analysis. Standards were prepared from a 100 ppm stock solution of Au ion (Perkin Elmer), from which 0.1 ml was mixed with 0.1 ml of 30  $\mu$ l HNO<sub>3</sub>/30  $\mu$ l HCl and diluted to 10 ml. Different volumes of 1 ppm stock were mixed with 0.1 ml of 2% HNO<sub>3</sub> and diluted to 1.0 ml to yield standards between 25 and 200 ppb. AA samples were burned at 130 °C for 60 s,

1000 °C for 45 s, and atomized at 1800 °C with a 5-s reading window. No salt interference was observed.

#### EXAMPLE 2. 2.6 nm-diameter colloidal Au

5           ml of 1 %  $\text{HAuCl}_4$  was added to 90 ml of  $\text{H}_2\text{O}$  at room temperature (20-23 °C). After one minute of stirring, 2.00 ml of 38.8 mM  $\text{Na}_3\text{citrate}$  was added. One minute later, 1.00 ml of fresh 0.075%  $\text{NaBH}_4$  in 38.8 mM  $\text{Na}_3\text{citrate}$  was added. The colloidal solution was stirred for an additional 5 minutes and stored in a dark bottle at 4 °C. TEM images of the 2.6-nm diameter colloidal gold particles are shown in Figure 9.

#### EXAMPLE 3. Citrate-seeded colloidal Au

10           To a stirred solution of boiling 0.01 %  $\text{HAuCl}_4$ , seed colloids (either 2.6-nm diameter or 12-nm diameter) were added coincidentally with the addition of 38.8 mM  $\text{Na}_3\text{citrate}$  (final concentration  $\approx 0.17$  mM). This mixture was boiled for 15 minutes and stirred for an additional 10 minutes while cooling. Citrate-seeded colloids were prepared in volumes ranging from 50 ml to 500 ml, with different diameters were generated by changing the volume of seed colloid added.

#### EXAMPLE 4. $\text{NH}_2\text{OH}$ -seeded colloidal Au

20           These syntheses utilized stock solutions of 1 %  $\text{HAuCl}_4$  and 40 mM  $\text{H}_2\text{NOH}$ , diluted to final concentrations as described in the Brief Description of the Figures. Except where noted, seed particles were added to stirred mixtures of  $\text{NH}_2\text{OH}$  and  $\text{HAuCl}_4$ .

#### EXAMPLE 5. Instrumentation for Analysis of Colloidal Metal Nanoparticles

25           Optical spectra were obtained on an HP8452A diode array UV-Vis spectrophotometer with a deuterium lamp (350 - 820 nm range, 2 nm resolution). Graphite furnace atomic absorption was performed with a Perkin-Elmer 11008 spectrophotometer, an HGA 700 power supply, an AS-70 autosampler and a Au lamp (Perkin Elmer). Equipment and protocols for acquisition and analysis of transmission electron microscopy (TEM) images have been described in Grabar, et al., *Anal. Chem.* 1995, 67:735-43; Bright, et al., *Langmuir* 1996, 12:810-17; Freeman, et al., *Science* 1995, 267:1629-32; Grabar, et al., *Langmuir* 1996, 12:2523-61; and Grabar, et al., *Anal. Chem.* 1997, 69:417-477; each specifically incorporated

30

by reference. Software protocols that allowed 2-D clusters of particles to be separated into individual entities (or when this was not possible, eliminated from consideration) were employed.

## 5 EXAMPLE 5. Film Growth

Colloidal Au nanoparticles measuring  $12 \pm 1$  nm in diameter were prepared, sized by TEM/image analysis, and assembled into 2-D arrays on silanized glass substrates according to methods described in Grabar, et al., *Anal. Chem.* 1995, 67:735-43; Bright, et al., *Langmuir* 1996, 12:810-17 and Freeman, et al., *Science* 1995, 267:1629-32. Au colloid multilayers  
10 were made by taking 12-nm diameter colloidal Au monolayers (immobilized on MPTMS-coated glass) and immersing them for 10 minutes in 10 mM 2-mercaptoethylamine. After exhaustive rinsing with H<sub>2</sub>O the surfaces were immersed in a fresh solution of 17 nM, 12-nm diameter colloidal Au nanoparticles for one hour. This process was repeated between 3-8 times (as indicated in the text).

15 In brief, hydroxylamine reduced Au metal films were developed on colloidal monolayers in 600 mL of 0.01 % HAuCl<sub>4</sub>/0.4 mM NH<sub>2</sub>OH on an orbital shaker. The surfaces were dried for optical spectra, conductivity measurements, AFM, FE-SEM and atomic absorbance.

More specifically, reduced Au metal films started from sets of Au colloid monolayers  
20 were prepared using either glass microscope slides (cut to 2.5 x 0.8 cm.) or glass microscope cover slips (2.5 x 2.5 cm). One side was wiped clean of colloid and the optical spectra were taken of the surface immersed in water. All monolayers were transferred to a solution of NH<sub>2</sub>OH in an 8 in. x 8 in. Pyrex dish and placed on a Lab-Line orbital shaker operated at 120 rpm. A solution of HAuCl<sub>4</sub> was added to initiate the reaction. All surfaces were exposed to  
25 the same reducing solution; samples were removed at regular intervals for subsequent characterization. After removal, surfaces were immediately washed in water, dried in a stream of Ar gas and stored in vials or Petri dishes. For each surface, an optical spectrum was recorded, after which two electrical contacts were deposited using a Circuit Works conductive pen from Planned Products. When the contacts dried, resistance between the contacts was  
30 measured and then the surfaces were imaged by AFM. At least two 5  $\mu$ m x 5  $\mu$ m scans and eight 1  $\mu$ m x 1  $\mu$ m images were collected from each surface; for FE-SEM, two 5  $\mu$ m scans and two 1  $\mu$ m scans were taken for each surface.

**EXAMPLE 6. Instrumentation for Analysis of Colloidal Au Monolayers**

Optical spectra were acquired on either an HP8452 UV-Vis connected to a Swan 386 (IBM compatible) or a Perkin-Elmer Lambda 9 spectrophotometer connected to a Gateway 486 (IBM compatible), using software supplied by the manufacturer. Resistance measurements were made with a Fluke 77 multimeter. Atomic absorbance measurements were made using a Perkin Elmer 11008 Graphite Furnace atomic absorption spectrophotometer.

SERS spectra were also collected using a Detection Limited microRaman system which consists of a Solution 633 Helium-Neon laser with a distal probe connected by fiber optic cable. The CCD and data collection were controlled by a Monorail PC clone running DLSPEC software. The lens used had a working distance of 3 mm, resulting in a spot size of approximately 5  $\mu\text{m}$ . The band pass for the microRaman system is  $\approx 8 \text{ cm}^{-1}$ . Data were processed and analyzed using GRAMS 32 software. Spectra were collected at 632.8 nm. All samples were run at 23 mW with 10-s integration time.

AFM images were acquired using a Digital Instruments Nanoscope IIa in tapping mode at a frequency of 1-2 Hz, and 512 lines per image using standard Si cantilevers from Digital Instruments. TEM images were taken in a JEOL model 1200EXII operated at 80 kV accelerating voltage and 100K magnification. FE-SEM images were acquired on a JEOL JSM 6320E at 3.0 kV accelerating voltage and 100K magnification.

SPR spectra were obtained on surfaces of dimensions 2.5 x 2.5 cm with a hemispherical prism (index of refraction  $\approx 1.515$ ) illuminated by a Spectra-Physics model 127 HeNe gas laser. Data was collected with a Newport photodiode (1 ns rise time) and a Stanford Research optical chopper and 530 lock-in amplifier. The instrument was operated by in-house written Labview 4.0 software operated by a Power Computing PowerCenter 150.

All electrochemical measurements were carried out using a PAR Model 273A Potentiostat/Galvanostat operated with Model 270 Software on a Gateway 486 IBM-compatible computer. All electrochemical measurements were taken in a beaker with the working electrode hanging in solution. Electrochemical solutions consisted of 5 mM  $[\text{Ru}(\text{NH}_3)_6]\text{Cl}_3$  in 0.1 M  $\text{Na}_2\text{SO}_4$ . The sample was scanned four times with the fourth scan being saved.

EXAMPLE 7. Colloid Preparation for Construction and Characterization of Colloidal Au and Ag Multilayers

All glassware used for colloid preparation was thoroughly cleaned in aqua regia (3 parts HCl, 1 part HNO<sub>3</sub>), and rinsed in deionized H<sub>2</sub>O prior to use. 12 nm Au colloid was prepared by citrate reduction of HAuCl<sub>4</sub> as described previously. The resulting solution of colloidal particles had an absorption maximum at 518 nm. Sample analysis by transmission electron microscopy (TEM) indicated an average particle with major axis diameter of 10.7 nm  $\pm$  1.3 nm and minor axis of 9.4 nm  $\pm$  1.1 nm from 221 particles sampled using NIH image software.

Large colloidal Au was prepared using a modified "seed colloid" technique. One ml of 14 nm colloid was used as the starting material to which were added 100 ml of 0.01% HAuCl<sub>4</sub> and 500 ml of citrate. The resulting sample as analyzed by TEM showed a major axis of 46.8 nm  $\pm$  5.4 nm and a minor axis of 38.6 nm  $\pm$  3, using 239 particles sampled using the NIH image software.

Polydisperse colloidal Ag was prepared as in Bright, et al., *Langmuir* 1998, 14:5695-5701; and Lee, et al., *J. Phys. Chem.* 1982, 86:3391-3395; using EDTA reduction of aqueous AgNO<sub>3</sub>. The Ag hydrosol produced had an intense plasmon absorption band at 402 nm.

EXAMPLE 8. Synthesis of Diisocyanophenylene Crosslinkers:

Proton nuclear magnetic resonance spectra (<sup>1</sup>H NMR) were obtained at 300 MHz on a Bruker AM-300 spectrometer. Diffuse reflectance Fourier transform infrared spectra (DRIFT) were obtained on a Mattson Galaxy FT-IR. Electron ionization mass spectra (EIMS) were obtained on a Kratos MS25. Analytical thin-layer chromatography was performed using precoated silica gel (60 F<sub>254</sub>) on aluminum plates obtained from Aldrich Chemical Company (St. Louis MO). Flash column chromatography was performed using Merck silica gel (grade 9385, 230-400 mesh, 60 Å) according to the procedures of Still et al., *J. Org. Chem.* 1978, 43:2923-2925. Benzidine and chloroform were obtained from Sigma Chemical Company (St. Louis MO). 4,4'-Diamino-*p*-terphenyl was obtained from Lancaster Synthesis Inc. (Windham NH). Benzyltriethylammonium chloride and magnesium sulfate were obtained from Aldrich. Potassium hydroxide was obtained from EM Science (Gibbstown NJ). Dichloromethane was obtained from Mallinckrodt (Phillipsburg NJ).

1,4-Diisocyanobenzene (1):

Diisocyanide **1** was obtained from Aldrich Chemical Company and used without further purification.

4,4'-Diisocyno-*p*-biphenylene (**2**):

Diisocyanides **2** and **3** were prepared using a modification of Henderson, et al.,

5 *Inorg. Chim. Acta* 1996, 242:115-125. 750 mg of Benzidine dissolved in 450 ml of CH<sub>2</sub>Cl<sub>2</sub> was placed in a 1000 ml, three-neck, round-bottomed flask equipped with a reflux condenser, magnetic stirbar and N<sub>2</sub> inlet. Into a 250 ml round-bottomed flask was placed 187.5 ml of a 50:50 (by weight) solution of KOH in H<sub>2</sub>O. The solutions were degassed for 15 min, then combined, along with 5 mg of benzyltriethylammonium chloride dissolved in 2.5 ml CHCl<sub>3</sub>.  
10 The reaction mixture was refluxed for 4.5 to 5.5 h under constant stirring, adding an additional 2.5 ml of CHCl<sub>3</sub> after 2 h. The mixture was then added to 450 ml of H<sub>2</sub>O and the organic layer extracted in a separatory funnel and washed twice with 450 ml H<sub>2</sub>O and once with 450 ml saturated NaCl solution. The CH<sub>2</sub>Cl<sub>2</sub> was dried over MgSO<sub>4</sub>, filtered, and evaporated in a rotary evaporator yielding a light brown crude product in 85% yield. TLC  
15 analysis, using 10% hexane in CH<sub>2</sub>Cl<sub>2</sub>, revealed that some monosubstituted 1-amino-4-isocyanobiphenylene was present. Both products were isolated using flash column chromatography with the 1:9 hexane/CH<sub>2</sub>Cl<sub>2</sub> solution as the solvent. The more soluble light yellow, powdery product was removed from the column yielding 405.0 mg (54%) of **2**. R<sub>f</sub>: 0.523; IR (KBr): ν(NC), 2128 cm<sup>-1</sup>; <sup>1</sup>H NMR (300 MHz, CDCl<sub>3</sub>): δ 7.49 (d, 4H), 7.63 (d, 4H); EIMS m/z: 204.2.  
20

4,4'-Diisocyno-*p*-terphenylene (**3**)

Diisocyanide **3** was prepared from the corresponding amine in a similar manner as described for **2**, with an 82% crude product yield and a 334.5 mg (44.6%) yield after chromatography. R<sub>f</sub>: 0.786; IR (KBr): ν(NC), 2130 cm<sup>-1</sup>; <sup>1</sup>H NMR (300 MHz, CDCl<sub>3</sub>): δ 7.43 (d, 4H), 7.59 (d, 4H), 7.63 (s, 4H); EIMS m/z: 280.1.  
25

EXAMPLE 9. Preparation of colloidal metal multilayers

Au colloid multilayer samples were constructed for surface plasmon resonance, electrochemical, electrical, and optical characterization by the following procedures. For  
30 electrode construction; In-doped SnO<sub>2</sub> (Delta Technologies) was degreased by 15 min. sonication in hexane, methanol, and H<sub>2</sub>O. A Cu wire was attached via conductive Ag epoxy (Epoxy Technologies), a glass tube was inserted over the wire, and white Dexter Epoxi-Patch was used to attach the tube to the In-doped SnO<sub>2</sub> and cover the Ag epoxy. The electrode

surface was silanized in a 3% MPTMS methanolic solution for 30 min., rinsed copiously with H<sub>2</sub>O and placed in a colloidal Au solution ( $11 \pm 1$  nm diameter particles) for 45 minutes. Multilayer assembly began by immersion of the electrode into 10 mM 2-mercaptoethanol for 15 min., followed by extensive rinsing, and reimmersion into Au colloid. The process was repeated with optical spectra and cyclic voltammograms were recorded after each iteration.

Samples for electrical and NIR analysis were prepared on Fisher Premium microscope slides cut to approximately 0.9 cm x 2.5 cm rectangles. Substrates were cleaned with aqua regia (3:1 HCl:HNO<sub>3</sub>), submerged in piranha wash (3:1 H<sub>2</sub>SO<sub>4</sub>:30% H<sub>2</sub>O<sub>2</sub>) and rinsed with H<sub>2</sub>O. Substrates were modified with silane and multilayers were constructed by alternate immersions into colloidal Au and a bifunctional crosslinker solution [5 mM 2-mercaptoethanol or 2-mercaptoethylamine in H<sub>2</sub>O, 1,6-hexanedithiol in CH<sub>3</sub>CH<sub>2</sub>OH, or 1, 2, 3 in CH<sub>2</sub>Cl<sub>2</sub>]. A vigorous rinse with H<sub>2</sub>O is necessary between each step. Four Au bars (100 nm) at 0.5-cm and 1-cm spacing were evaporated across the width of the slide to provide contact for resistance measurements.

In the case of multilayers made with two different sizes of Au colloid, the above procedure was followed with the exception that the substrates were put into the 46-nm diameter colloid for 20 h. In addition, the solution was gently agitated to increase the diffusion of colloids to the surface.

Ag monolayers were prepared as followed: clean glass substrates were silanized by reaction with 10% MPTMS in CH<sub>3</sub>OH for 1-2 h., followed by extensive rinsing with CH<sub>3</sub>OH and H<sub>2</sub>O and exposure to colloidal Ag solution for 1-1.5 h. Multilayers were prepared from monolayers by treatment with 4 mM BME for 8-10 minutes, followed by extensive rinsing and exposure to colloidal Ag for 1-1.5 h. This process was repeated 0-9 times to produce surfaces with increasing amounts of Ag. Surfaces were rinsed in H<sub>2</sub>O, then CH<sub>3</sub>OH, and dried in an 80 °C oven before storage in air.

Mixed-metal (Au/Ag) multilayers were prepared in a similar fashion to Ag multilayers, except that either Au or Ag colloid was used when Ag sol was used in the above description. All of the initial monolayers were Au colloid on APTMS (10% CH<sub>3</sub>OH). Surfaces were dried as described for Ag multilayers.

#### EXAMPLE 10 Preparation of Au Films by Evaporation

Thin (47-50 nm) Au films were prepared by thermal evaporation of Au shot (99.99%, Johnson Mathey) from a resistively-heated Mo boat (Kurt J. Lesker) in a diffusion-pumped



Edwards Auto 306 thin film fabrication system. Evaporation substrates were 1" x 1" x 0.02" pieces of polished SF11 glass ( $n = 1.78$ , Schott Glass Technologies) that had been exposed to a 10% (v/v) 3-mercaptopropyltrimethoxysilane/ $\text{CH}_3\text{OH}$  solution for 30 minutes in order to increase the adhesion of Au to the glass. Au was deposited at a pressure of  $1 \times 10^{-6}$  mbar at 0.5 nm/s with constant sample rotation to ensure uniform deposition. Following evaporation, the films were annealed in a home-built glass tube oven at 300 °C for 5-10 minutes under a constant flow of Ar to decrease the surface roughness of the evaporated layer.

#### EXAMPLE 11: Instrumentation for Analysis of Colloidal Metal Multilayers

Optical spectra were recorded on a HP-8452 diode array Uv-Vis or an Perkin-Elmer Lambda 9 scanning Uv-Vis/NIR. Au colloid coverage was calculated from atomic absorption spectrometry data from a Perkin-Elmer 110013 AAS. The sample area (6 mm diam.) was confined within a glass cell (O-ring sealed), digested in 50% aqua regia, and diluted to a known volume with  $\text{H}_2\text{O}$ . A Digital Instruments Nanoscope 3A operated in tapping-mode at 2 Hz scan rate and 512 lines per image was used to acquire topography scans and electric field measurements. A Princeton Applied Research model 273 potentiostat was used to collect cyclic voltammograms. 2 mm Au bars (1000A) were sputter coated onto each end of a partially masked multilayer using a Balzer SCD-050 sputterer. Conductivity measurements were made in typical 2-point fashion using a homebuilt sample holder. A Keithley 6517A high resistance electrometer or Fluke 77 multimeter was used to collect resistance data. UV light was generated with a Boekel Industries Uv-Clean (model 135500).

SERS spectra were obtained by irradiating a sample with 107 mW of power from a Coherent Innova-70 Spectrum Laser (mixed Ar/Kr) at 647.1 nm. Scattered light was collected in a backscattering geometry and focused into a SPEX 1877 triple monochromator fitted with a 1200 gr/mm grating in the spectrograph stage and two 600 gr/mm gratings in the filter stage. The bandpass was  $5 \text{ cm}^{-1}$ . Detection was with a CCD detector cooled to 140 K. The spectrometer was calibrated using imidazole as a frequency standard. Each spectrum is the average of 10 acquisitions integrated for 10 s each.

Surface plasmon curves were measured using a homebuilt high-resolution scanning SPR instrument. Excitation of the surface plasmon was accomplished using the Kretschmann geometry where a 1" diameter hemispherical prism (SF11 glass, Esco Products) is index matched (Cargille Immersion Oil,  $n = 1.78$ ) to a SF11 substrate onto which Au had been previously evaporated. This assembly was then affixed to a home-built flow cell (volume =

100 ml) with the Au film was exposed to solution. The SPR excitation source was a cylindrical 5 mW, 500:1 polarization extinction HeNe laser (632.8 nm, Melles Griot) which is further polarized by a 500:1 visible-optimized linear polarizer. An optical chopper (Stanford Research Systems) was used to modulate the optical signal at a frequency of 2 kHz  
5 that was then correlated with detection via a lock-in amplifier (Stanford Research Systems). The beam was focused by a 100-mm focal length (fl) plano-convex (PCX) lens and recollimated by a 25-mm fl PCX lens, thereby reducing the beam size to  $0.4 \pm 0.1$ -mm in diameter. A hemispherical lens was then used to focus the beam such that it was recollimated by the hemispherical prism-sample assembly. The reflected beam was then passed through  
10 an iris and focused onto a silicon photodiode detector (Thor Labs), the signal from which was then measured with the lock-in amplifier that was in-phase with the excitation source. Angular positioning of the sample was accomplished with a home-built 0-26 stage consisting of two high-resolution ( $0.001^\circ$ ) servo-drive rotation stages (Newport Corp.) that are mounted together such that their axes of rotation are co-linear. The prism/sample/flow cell assembly  
15 was then mounted on the 0-20 stage such that the center of the Au/glass sample was at the axis of rotation. Stage rotation and data collection are controlled through a computer interface that is developed in-house with the LabVIEW programming language (v. 4.01, National Instruments). Typical SPR scan were run at either  $0.1^\circ$  or  $0.01^\circ$  resolution, a stage rotation rate of  $0.5^\circ \text{ s}^{-1}$ , and a lock-in time constant of 0.3 s.

Table 1. Physical Properties of Colloidal Au Nanoparticles Prepared by Direct Citrate Reduction and By Citrate Seeding of 2.6-nm Diameter and 12-nm Diameter Colloidal Au Solutions

	Batch	Major Axis x Minor Axis <sup>a</sup>	G <sup>b</sup>	$\lambda_{\max}$ (nm)	Peak Width (nm)	Source of Colloid
<i>Small seeds</i>		2.6 (1.0) x 2.0 (0.8)	1.30	514	104	this work
<i>Large seeds</i>		12.6 (1.1) x 11.5 (1.0)	1.10	518	84	this work
<b>Synthetic Method</b>						
<i>Direct Citrate</i>	1	21 (2.3) x 19 (2.3)c	1.13	524	83	Goodman
	2	22.3 (5.0) x 18.6 (2.4)	1.20	528	116	this work
	3	25 (3.3) x 21 (3.3)	1.19	524	90	Goodman
	4	31.7 (7.6) x 24.5 (3.9)	1.29	530	136	this work
	5	35 (4.0) x 26 (4.0)	1.33	530	108	Goodman
	6	44 (6.9) x 33 (6.9)	1.34	528	104	Goodman
	7	44.9 (9.5) x 36.4 (5.6)	1.23	524	118	this work
	8	48 (10.5) x 37 (10.5)	1.31	535	98	Goodman
	9	56 (8.4) x 41 (8.4)	1.37	535	147	Goodman
<i>Seeded, Large</i>	1	19.3 (1.7) x 16.4 (1.1)	1.18	520	84	this work
	2	21.4 (2.6) x 18.5 (1.9)	1.16	522	80	this work
	3	25.0 (2.2) x 21.3 (1.6)	1.17	524	80	this work
	4	28.7 (2.6) x 24.3 (2.0)	1.18	526	76	this work
	5	31.1 (3.5) x 26.0 (2.4)	1.20	526	82	this work
	6	38.4 (4.7) x 31.8 (2.7)	1.21	528	78	this work
	7	44.5 (5.8) x 36.8 (4.1)	1.21	530	84	this work
	8	53 (4.8) x 43 (3.1)	1.23	534	92	this work
	9	64 (6.3) x 51 (3.8)	1.26	545	112	this work
	10	72 (9.4) x 54 (5.2)	1.33	542	152	this work
	11	76 (11) x 56 (6.0)	1.36	538	116	this work
	12	91 (14) x 68 (8.2)	1.35	550	220	this work
<i>Seeded, Small</i>	1	35.8 (8.7) x 30.6 (7.3)	1.17	548	188	this work
	2	36.4 (5.2) x 29.6 (3.1)	1.23	530	96	this work
	3	43.0 (7.8) x 36.8 (6.2)	1.17	534	132	this work
	4	53 (5.2) x 44 (3.7)	1.21	542	108	this work
	5	56 (7.2) x 45 (4.6)	1.25	544	144	this work
	6	61 (10) x 49 (7.5)	1.24	548	164	this work
	7	75 (17) x 60 (11)	1.24	548	216	this work
	8	93 (20) x 68 (11)	1.37	572	300	this work
	9	108 (38) x 77 (20)	1.40	548	300	this work
	10	111 (27) x 81 (17)	1.38	616	404	this work

<sup>a</sup>Values in parentheses are standard deviations; all values are in nm. <sup>b</sup>Ellipticity, as defined in text. <sup>c</sup>Grabar, et al., *Anal. Chem.* 1997, 69:417-477, gives a single standard deviation for a given preparation of particles, so it is used for both axes.

Table 2: Particle Size and Shape Analysis for Iteratively NH<sub>2</sub>OH-Seeded Colloidal Au Nanoparticles

Fig. 6 Panel <sup>a</sup>	Number Sized	Mean d Major x Minor <sup>b,c</sup>	Median d <sup>c</sup> Major x Minor	G (Mean)	Predicted Size <sup>c,d</sup> Major x Minor
<b>Total<sup>e</sup></b>					
<b>A</b>	1322	13.0(1.4)x11.8(1.2)	12.8x11.7	1.10	
<b>B</b>	2829	18.0 (2.7) x 16.3 (2.3)	17.8 x 16.1	1.10	
<b>C</b>	2263	35.1 (9.0) x 28.4 (3.6)	32.8 x 28.6	1.24	
<b>D</b>	3363	51.1(28.6) x 36.1 (5.4)	41.7 x 37.0	1.42	
<b>E</b>	917	65.8(31.0) x 49.5 (7.0)	56.0 x 49.9	1.33	
<b>F<sup>f</sup></b>	<sup>g</sup>	<sup>g</sup>	<sup>g</sup>	<sup>g</sup>	
<b>Spheres</b>					
<b>A</b>	1183	12.9 (1.3) x 11.9 (1.2)	12.7 x 11.7	1.08	
<b>B</b>	2630	17.9 (2.5) x 16.4 (2.3)	17.7 x 16.2	1.09	21.0 x 19.0
<b>C</b>	1964	32.4 (3.2) x 29.2 (2.7)	32.3 x 29.0	1.11	33.7 x 30.3
<b>D</b>	2839	41.1 (4.0) x 37.7 (3.5)	41.0 x 37.6	1.09	45.5 x 41
<b>E</b>	799	56.2 (5.4) x 51.0 (5.1)	55.3 x 50.4	1.10	59 x 53
<b>F</b>	1443	116 (11) x 102 (10)	116 x 102	1.14	121 x 103
<b>Rods<sup>e</sup></b>					
<b>A</b>	120	14.2(2.1)x11.6(1.7)	13.7x11.2	1.22	
<b>B</b>	100	20.8 (4.3) x 15.1 (1.9)	19.8 x 14.8	1.38	
<b>C</b>	200	58.9(12.8)x21.4 (3.2)	57.3x21.0	2.75	
<b>D</b>	399	122 (32.2) x 25.3 (3.9)	127.0 x 24.6	4.82	
<b>E</b>	80	145 (42.4) x 35.0 (7.0)	163.5 x 33.0	4.14	
<b>F</b>	200	236 (60.3) x 77.1 (9.6)	233.6 x 74.2	3.06	

<sup>a</sup>For convenience, solutions of seeded particles have been named according to their TEM image in Figure 6. <sup>b</sup>Numbers in parentheses refer to standard deviations. <sup>c</sup>In nanometers.

<sup>d</sup>With the exception of **B**, whose predicted size was based on the actual size of **A**, predictions were based on predicted sizes from the previous iteration. <sup>e</sup>"Total" refers to all the particles in a given batch of colloid, while "spheres" and "rods" refer those subsets of particles possessing the corresponding shapes. Particles with G > 1.2 were called rods. <sup>f</sup>F represents a two-step iteration from **E**. The predicted dimensions for the hidden iteration (**E'**) was 84 x 72 nm.



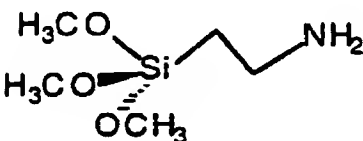


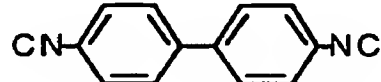
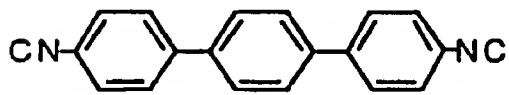
<sup>g</sup>The pronounced bimodality of the particle size distribution precluded meaningful calculation of mean diameter and ellipticity.

Table 3. Resistance of Au<sup>3+</sup>/NH<sub>2</sub>OH-Seeded Au Colloid Monolayers and Multilayers

Sample	Immersion Time (Minutes) <sup>a</sup>	Resistance( $\Omega$ ) <sup>b</sup>	Corresponding AFM Image
Low coverage Au monolayer <sup>c</sup>	1	insulating	
	3	insulating	Figure 10, Panel B
	6	650,000	Figure 10, Panel C
	7	370	Figure 10, Panel D
	8	120	
	9	40	Figure 10, Panel E
	30	4	Figure 10, Panel F
High coverage Au monolayer <sup>d</sup>	1	insulating	
	2	insulating	Figure 11, Panel B
	3	1000	Figure 11, Panel C
	4	100	
	5	56	Figure 11, Panel D
	6	14	
	8	5.6	Figure 11, Panel E
Au colloid multilayer <sup>e</sup>	17	0.5	Figure 11, Panel F
	1	9,700,000	
	2	6,000,000	
	4	30,000	
	10	40	

<sup>a</sup>In a 120 rpm orbital shaker loaded with 0.01% HAuCl<sub>4</sub>/0.4 mM NH<sub>2</sub>OH. <sup>b</sup>DC resistance as measured with a two-point probe. Measurement length was  $2.1 \pm 0.1$  cm; sample width was  $0.9 \pm 0.1$  cm. <sup>c</sup>12-nm diameter Au/MPTMS/glass. <sup>d</sup>12-nm diameter Au/MPTMS/glass. <sup>e</sup>12-nm diameter Au/MPTMS/glass followed by 3 treatments each with 2-mercaptoethylamine/17 nM, 12-nm diameter colloidal Au.

Table 4 Crosslinkers used form multilayers

Crosslinker	Length (Å)
	5.6 <sup>a</sup>
	8.0 <sup>a</sup>
	9.1 <sup>a</sup>
	9.5 <sup>a</sup>
	11.3 <sup>a</sup>
	12.4 <sup>a</sup>
	16.9 <sup>a</sup>
Bovine Serum Albumin	143 <sup>b</sup>
Horse Radish Peroxidase	140 x 40 x 40 <sup>c</sup>

<sup>a</sup>Energy minimized length<sup>b</sup>From structure described in Gajhede, et al., *Nat. Struct. Biol.* 1997, 4:1032-1035.5 <sup>c</sup>From crystal structure described in Bendedouch & Chen, *J. Phys. Chem.* 1983, 87; 1473-1477.

What is claimed is:

1. A method for preparing colloidal metal nanoparticles, comprising:
  - a) preparing a solution of a source of metal ions at boiling temperature;
  - 5 b) preparing a solution of reductant;
  - c) adding said solution of reductant coincidentally with seed colloids to said solution of a source of metal ions at boiling temperature to generate a seeding solution;
  - d) boiling said seeding solution; and
  - e) cooling said seeding solution;
  - 10 whereby colloidal metal nanoparticles are formed.
2. The method of Claim 1, wherein the source of metal ions is  $\text{HAuCl}_4$ .
3. The method of Claim 1, wherein the reductant is selected from the group consisting of citrate, malate, oxalate, aspartate, and glutamate.
4. The method of Claim 1, wherein the colloidal metal nanoparticles are colloidal  
15 gold nanoparticles.
5. The method of Claim 1, wherein said solution of a source of metal ions at boiling temperature is undergoing stirring, and steps c), d), and e) further comprise stirring.
6. A method for preparing colloidal metal nanoparticles, comprising:
  - a) preparing a solution of boiling  $\text{HAuCl}_4$  undergoing stirring having a  
20 concentration of about 0.01%;
  - b) preparing a solution of about 40 mM  $\text{Na}_3\text{citrate}$ ;
  - c) adding said solution of  $\text{Na}_3\text{citrate}$  coincidentally with seed colloids to said solution of  $\text{HAuCl}_4$  to generate a seeding solution undergoing stirring;
  - d) boiling said seeding solution undergoing stirring for about 15 minutes; and
  - 25 e) cooling said seeding solution undergoing stirring for about 10 minutes;
  - whereby colloidal metal nanoparticles are formed.
7. A method for preparing colloidal metal nanoparticles, comprising:
  - a) preparing a solution of  $\text{HAuCl}_4$ ;
  - b) preparing a solution of  $\text{NH}_2\text{OH}$ ;

c) mixing said solution of  $\text{HAuCl}_4$  with said solution of  $\text{NH}_2\text{OH}$  to produce a seeding solution;

d) adding seed colloids to said seeding solution;

whereby colloidal metal nanoparticles are formed.

5           8. The method of Claim 7, further comprising stirring the seeding solution prior to the addition of seed colloids.

9. The method of claim 7, further comprising repeating steps b) and c) up to six times.

10          10. The method of Claim 9, wherein the seed colloids are obtained from performing the method in an iterative fashion.

11. The method of claim 9, wherein the  $\text{HAuCl}_4$  solution has a concentration of about 1%, and the  $\text{NH}_2\text{OH}$  solution has a concentration of about 0.2 mM.

15          12. The method of claim 7, wherein the  $\text{HAuCl}_4$  concentration is about 0.01%, the  $\text{NH}_2\text{OH}$  concentration is about 40 mM, and the seed colloids are at a concentration of about 17 nM.

13. The method of Claim 12, wherein 3.2 mL of  $\text{HAuCl}_4$ , 0.1 mL of  $\text{NH}_2\text{OH}$ , and about 0.05 mL of seed colloids are used.

14. Colloidal metal nanoparticles with a major axis standard deviation of about 14%, or less a minor axis standard deviation about 14% or less, and an ellipticity  $< 1.5$ .

20          15. Colloidal metal nanoparticles with a major axis standard deviation of about 29% or less, a minor axis standard deviation of about 20% or less, and an ellipticity  $> 1.5$ .

16. A method for enlarging immobilized gold nanoparticles, comprising:

a) preparing an Au colloid monolayer;

b) preparing a solution comprising a source of  $\text{Au}^{3+}$

25          c) preparing a solution comprising a reductant;

d) immersing said Au colloid monolayer in said solution comprising a reductant;



e) adding said solution comprising a source of  $\text{Au}^{3+}$ ;  
whereby the immobilized gold nanoparticles are enlarged.

17. The method of Claim 16, wherein the solution comprising a reductant is stirred, and the solutions of steps d) and e) are stirred.

5 18. A method for preparing a gold film with features up to about 50 nm tall and about 75 nm wide comprising:

- a) preparing a low-coverage Au colloid monolayer;
- b) preparing a solution comprising a source of  $\text{Au}^{3+}$
- c) preparing a solution comprising a reductant;
- 10 d) immersing said Au colloid monolayer in said solution comprising a reductant;
- e) adding said solution comprising a source of  $\text{Au}^{3+}$ ;

whereby the gold film is prepared.

19. A method for preparing a gold film with features about 25 nm tall or less comprising:

- 15 a) preparing a high-coverage Au colloid monolayer;
- b) preparing a solution comprising a source of  $\text{Au}^{3+}$
- c) preparing a solution comprising a reductant;
- d) immersing said Au colloid monolayer in said solution comprising a reductant;
- e) adding said solution comprising a source of  $\text{Au}^{3+}$ ;

20 whereby the gold film is prepared.

20. A thin Au film having substantially similar conductivity to pure Au, prepared by the method of Claim 19.

21. A thin Au film useful as an a cyclic voltammetry electrode, prepared by the method of Claim 19.

25 22. A thin Au film whose nanostructure is indistinguishable from those of granular metal films prepared by evaporation, and having a mean roughness of about 3 nm rms, prepared by the method of Claim 19.

23. A thin Au film with increased SERS intensity, prepared by the method of Claim 19.

24. A thin Au film for which a reflectivity vs. excitation angle plot exhibits a pronounced minimum, prepared by the method of Claim 19.

- 5           25. A method for preparing a gold film multilayer comprising:
- a) preparing an Au colloid multilayer;
  - b) preparing a solution comprising a source of  $\text{Au}^{3+}$
  - c) preparing a solution comprising a reductant;
  - d) immersing said Au colloid monolayer in said solution comprising a reductant;
  - 10          e) adding said solution comprising a source of  $\text{Au}^{3+}$ ;

whereby the gold film multilayer is prepared.

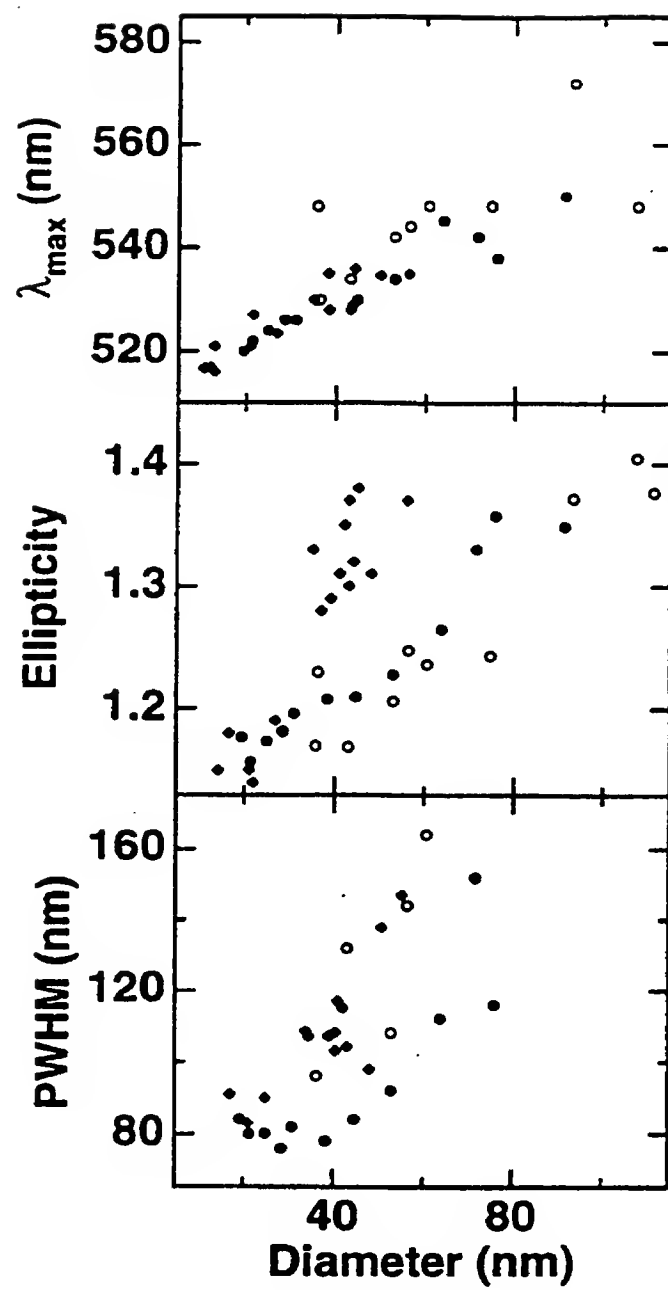


Fig. 1

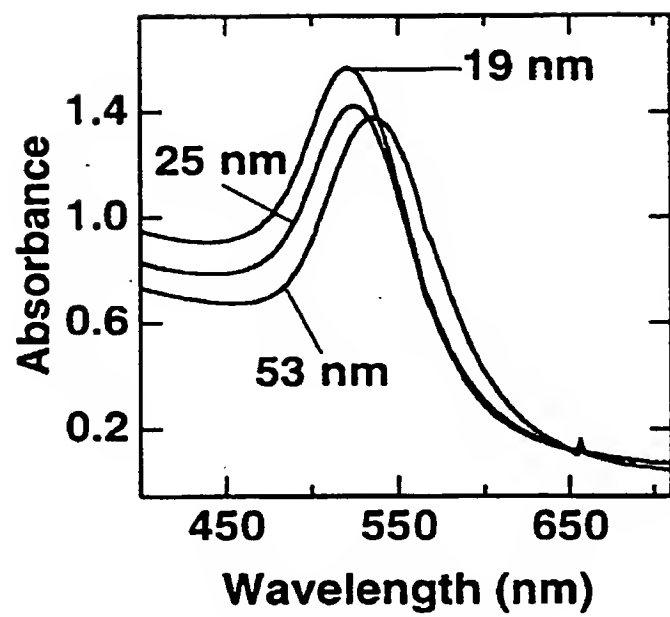


Fig. 2

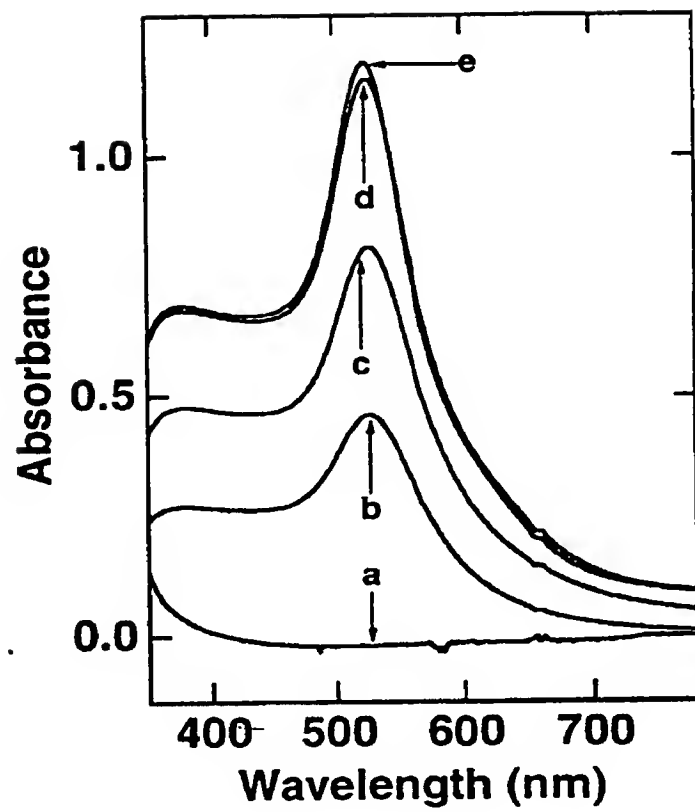


Fig. 3

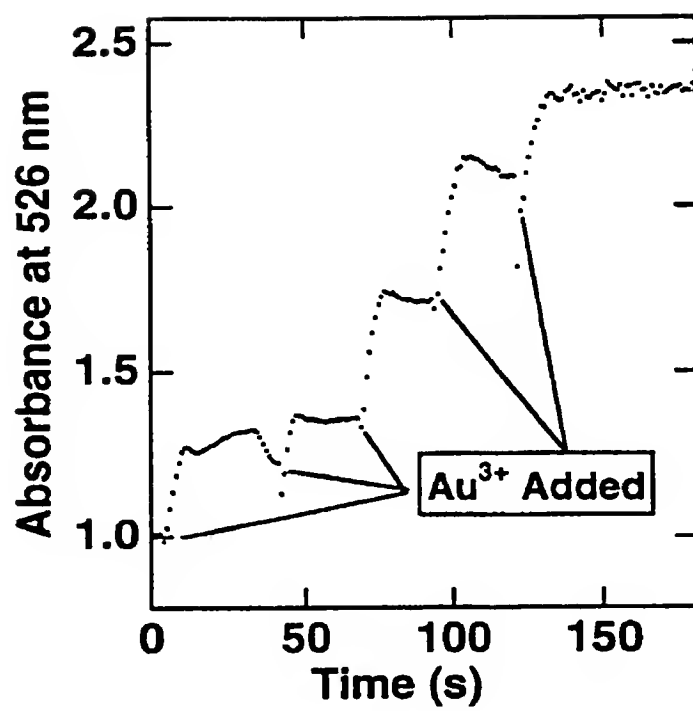
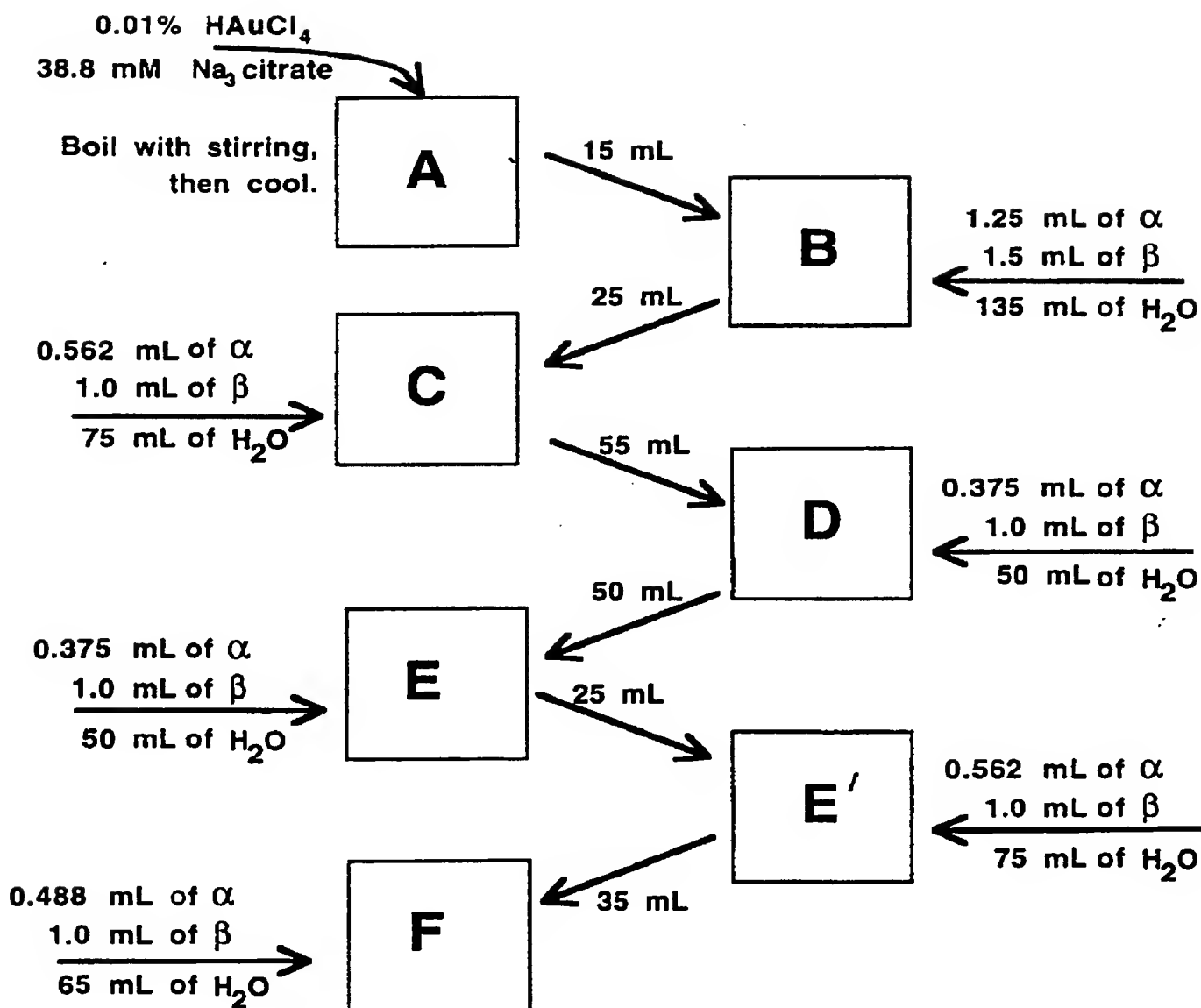


Fig. 4



**Supporting Information Scheme 1.** The process of iterative seeding used to produce the colloids discussed in Table 2. The initial colloid batch (A) was prepared by mixing boiling gold (III) with sodium citrate. Reagent  $\alpha$  is 0.2 M hydroxylamine hydrochloride and reagent  $\beta$  is 1.0 % hydrogen tetrachloroaurate. All subsequent colloids were made by mixing  $\alpha$  with colloid in the water and adding  $\beta$  to initiate the reaction. For example, 135 ml water, 1.5 mL of  $\alpha$  and 15 mL of colloid A were stirred and 1.25 mL of reagent  $\beta$  was added while stirring vigorously at room temperature.

Fig. 5

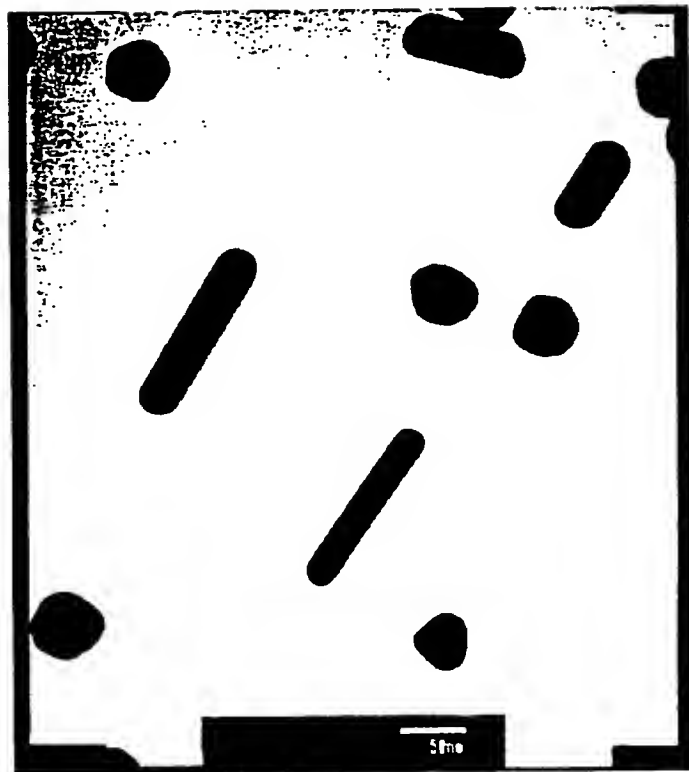


Fig. 6



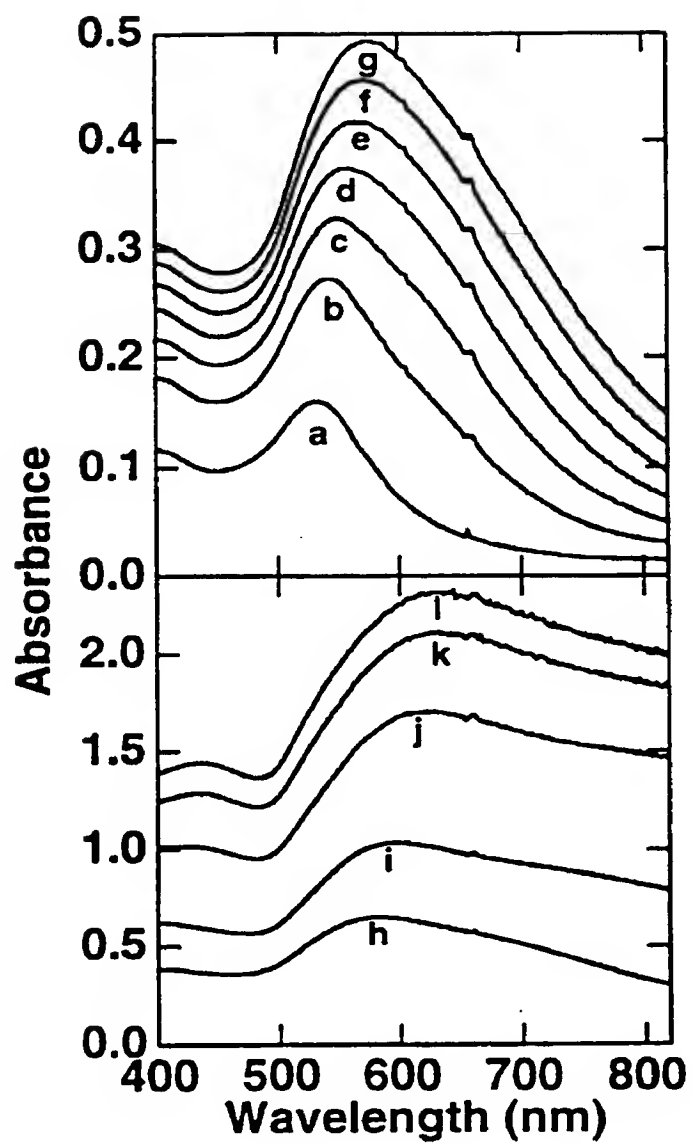


Fig. 7

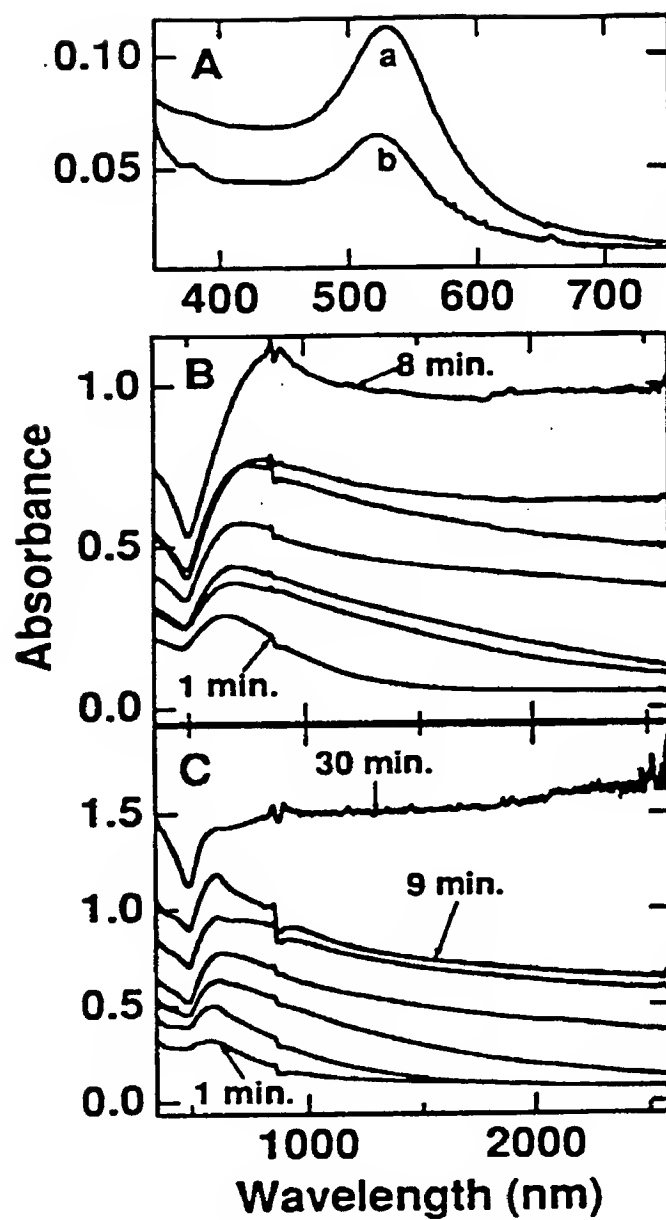


Fig. 8

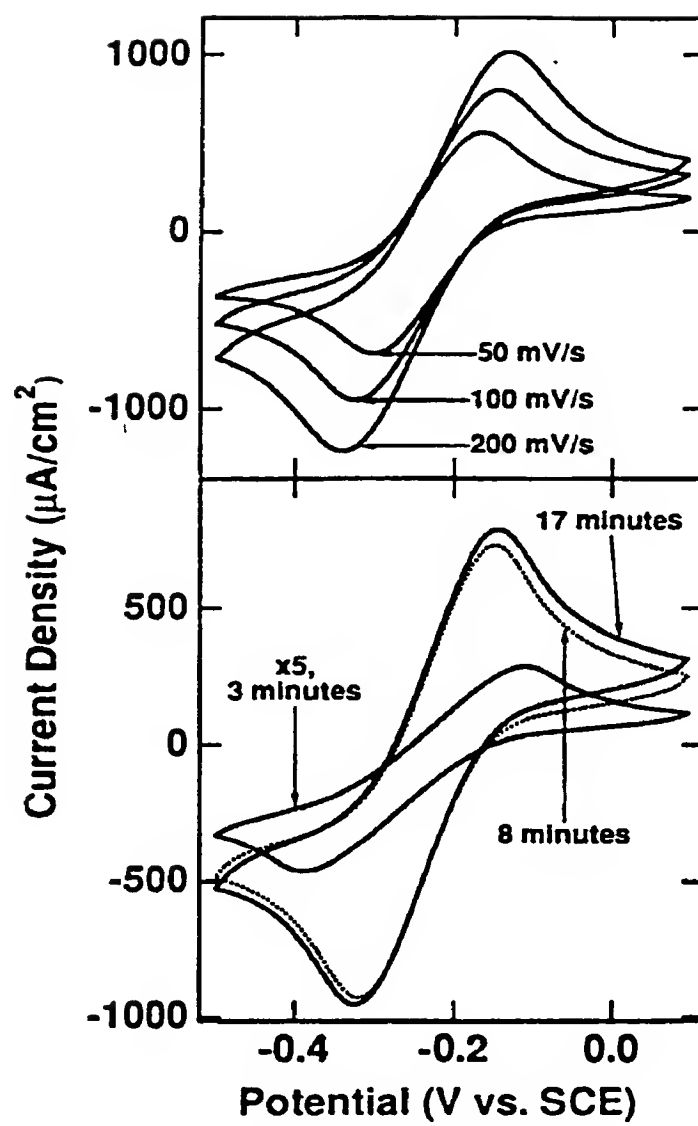


Fig. 9

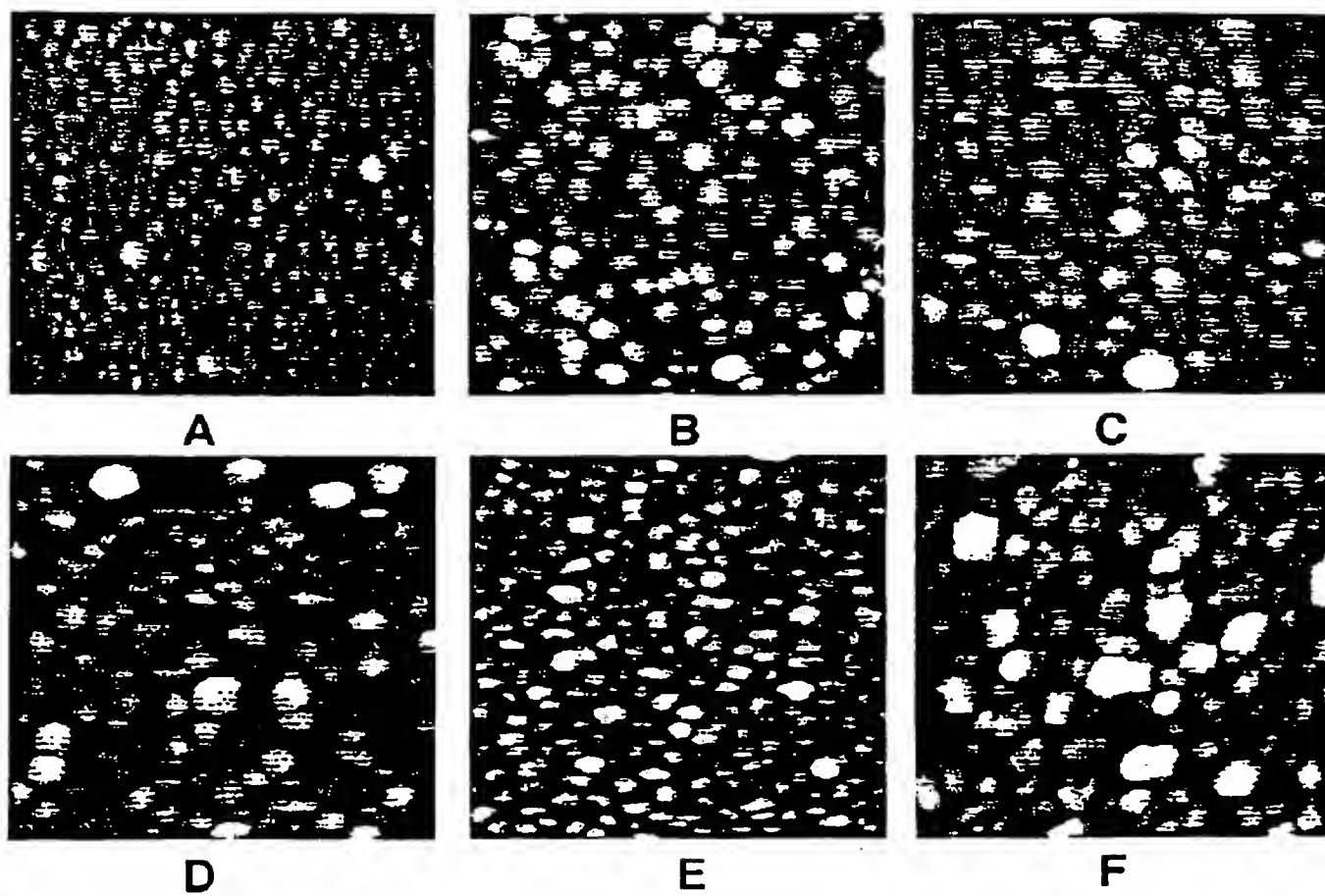


Fig. 10

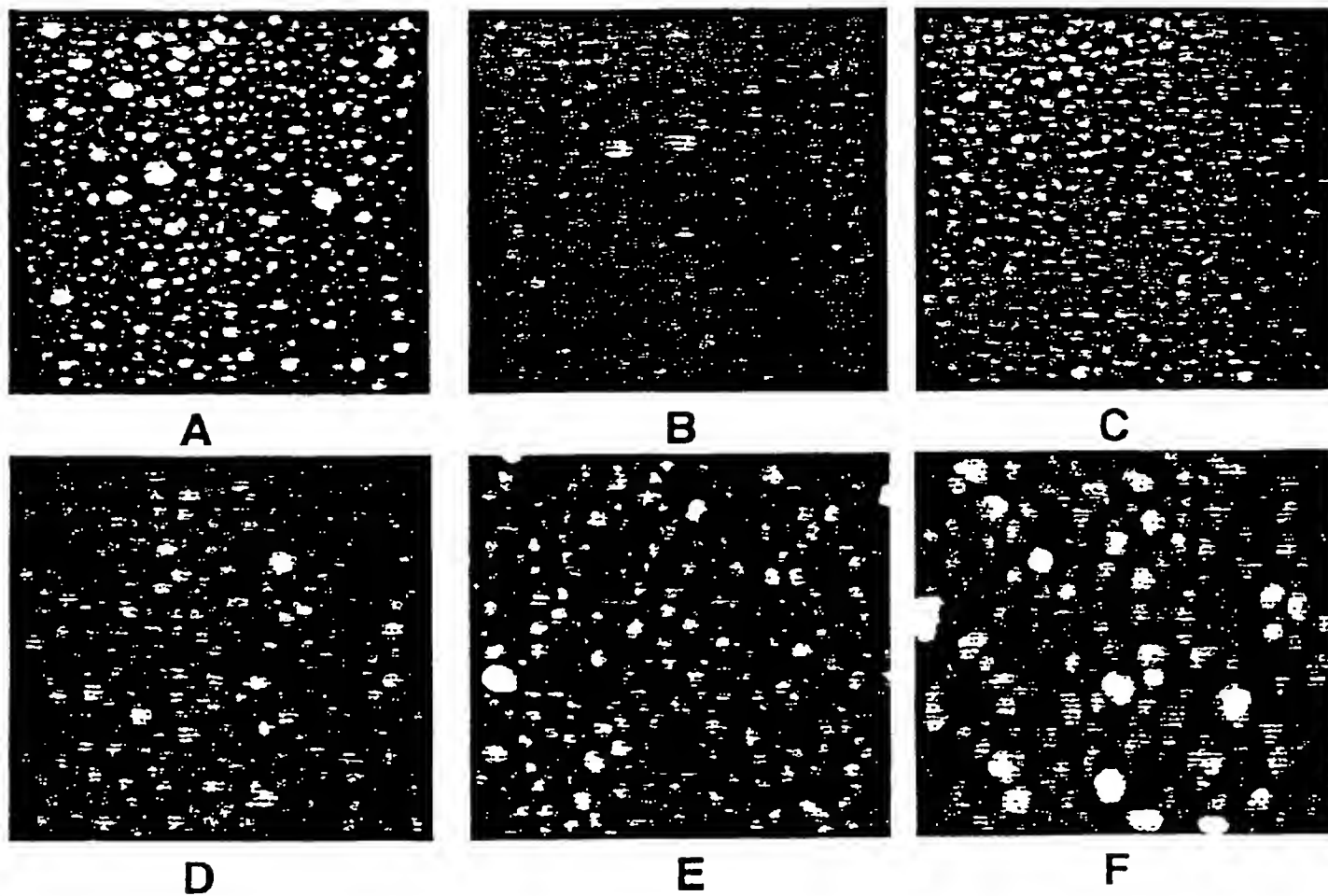


Fig. 11

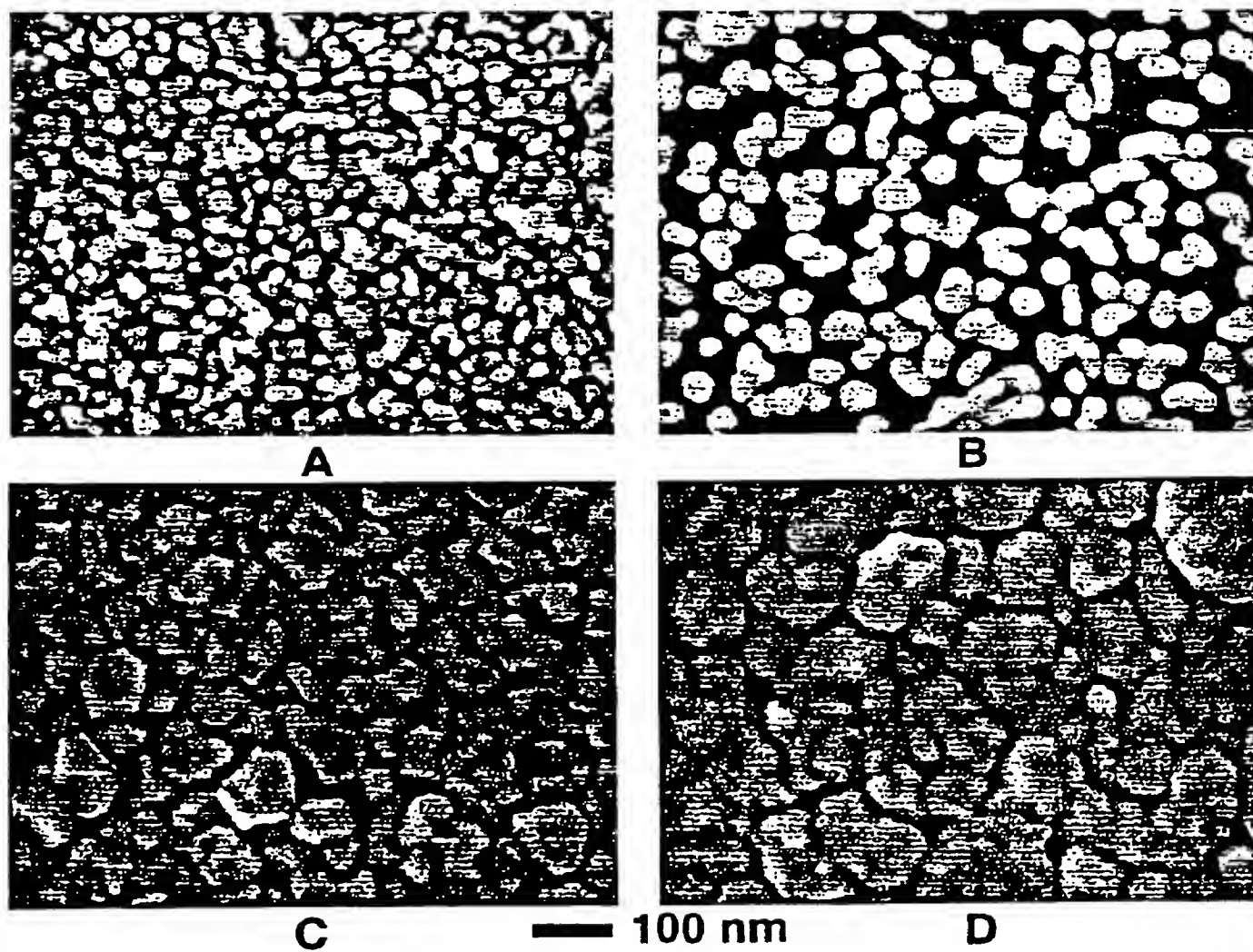


Fig. 12

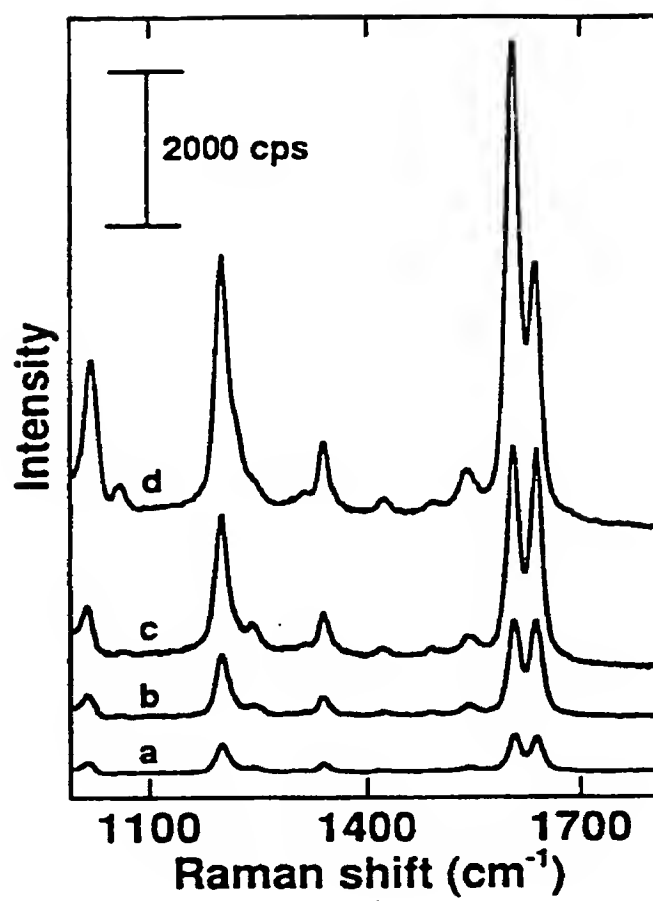


Fig. 13

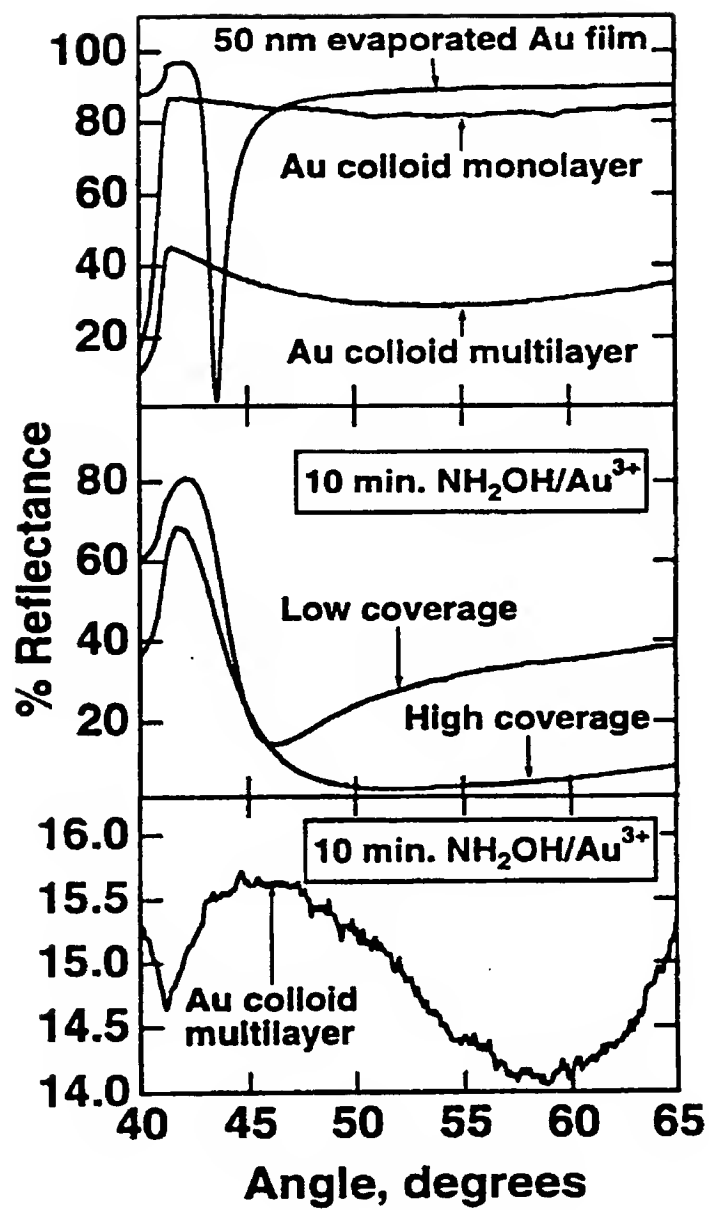


Fig. 14



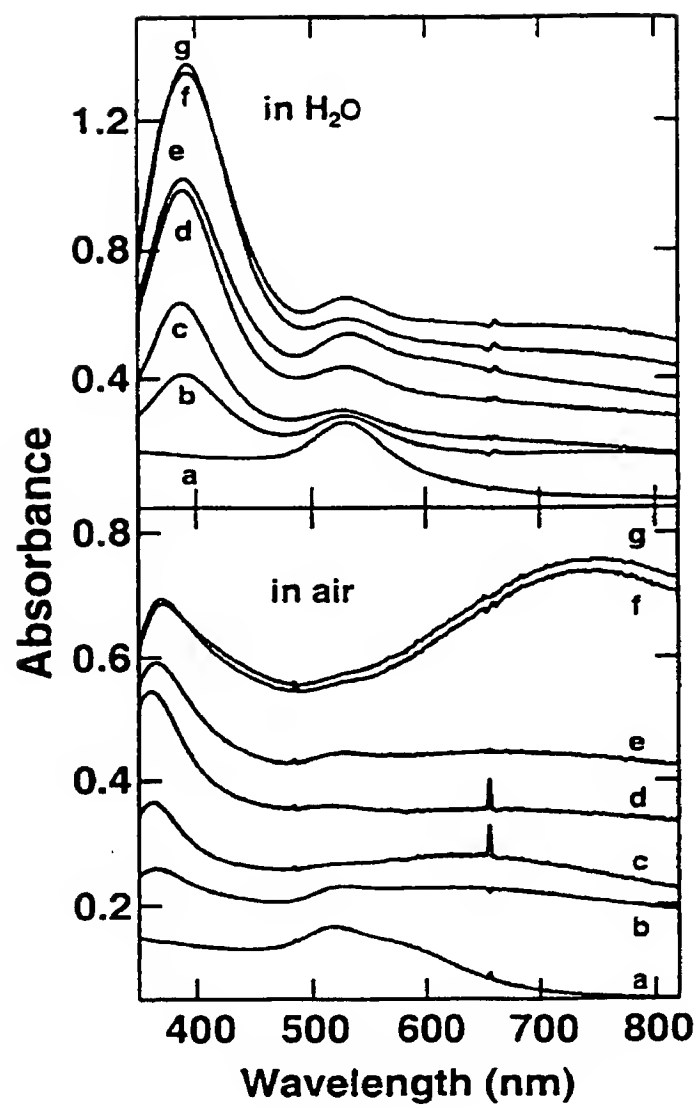


Fig. 15

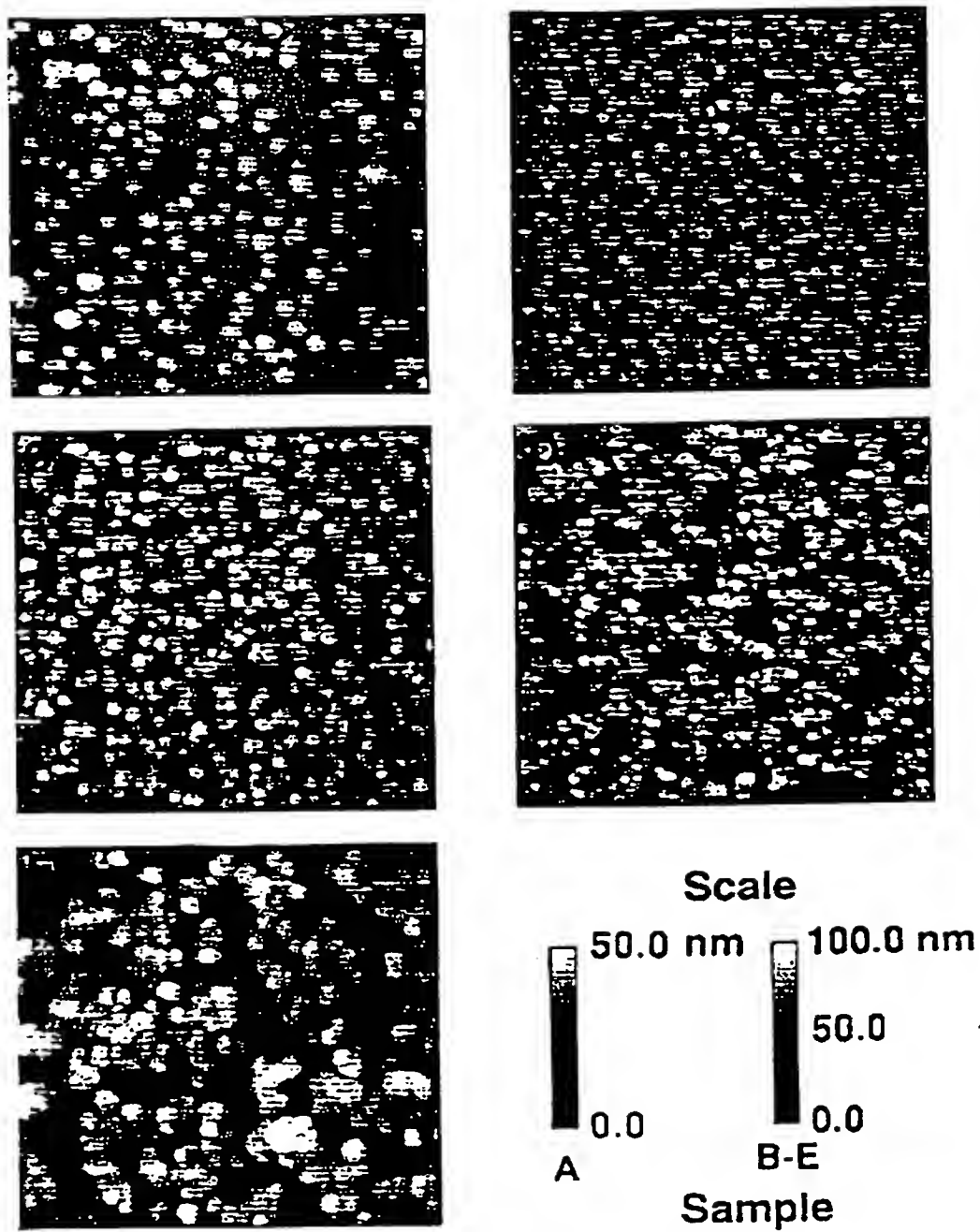


Fig. 16

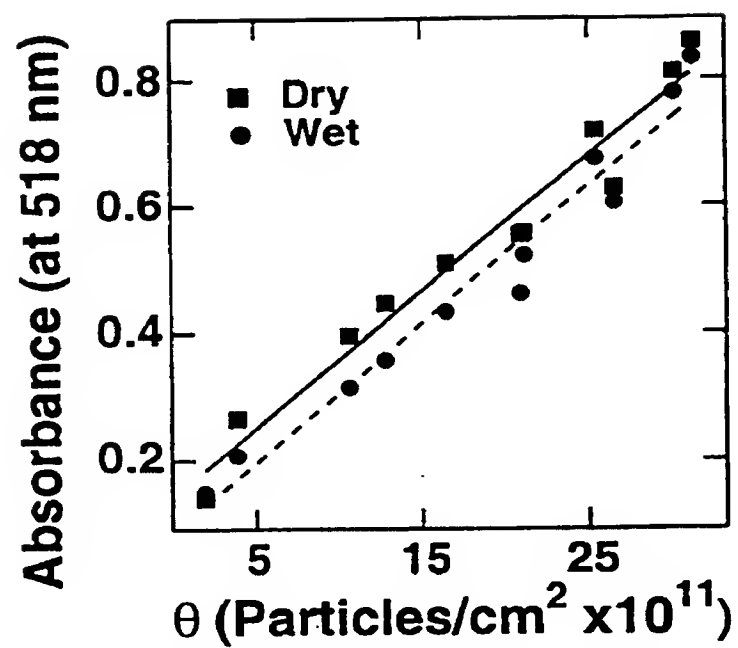


Fig. 17

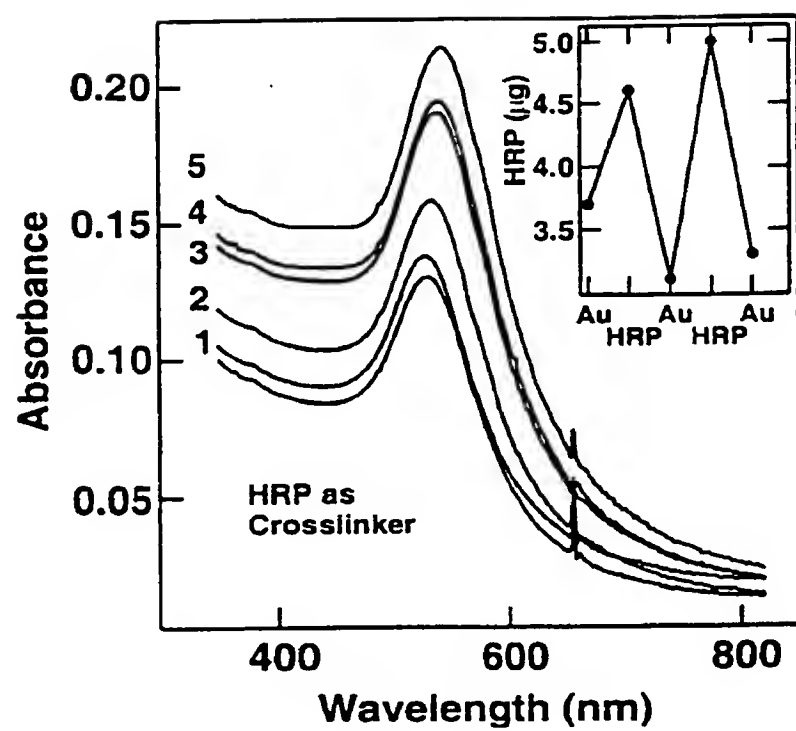


Fig. 18

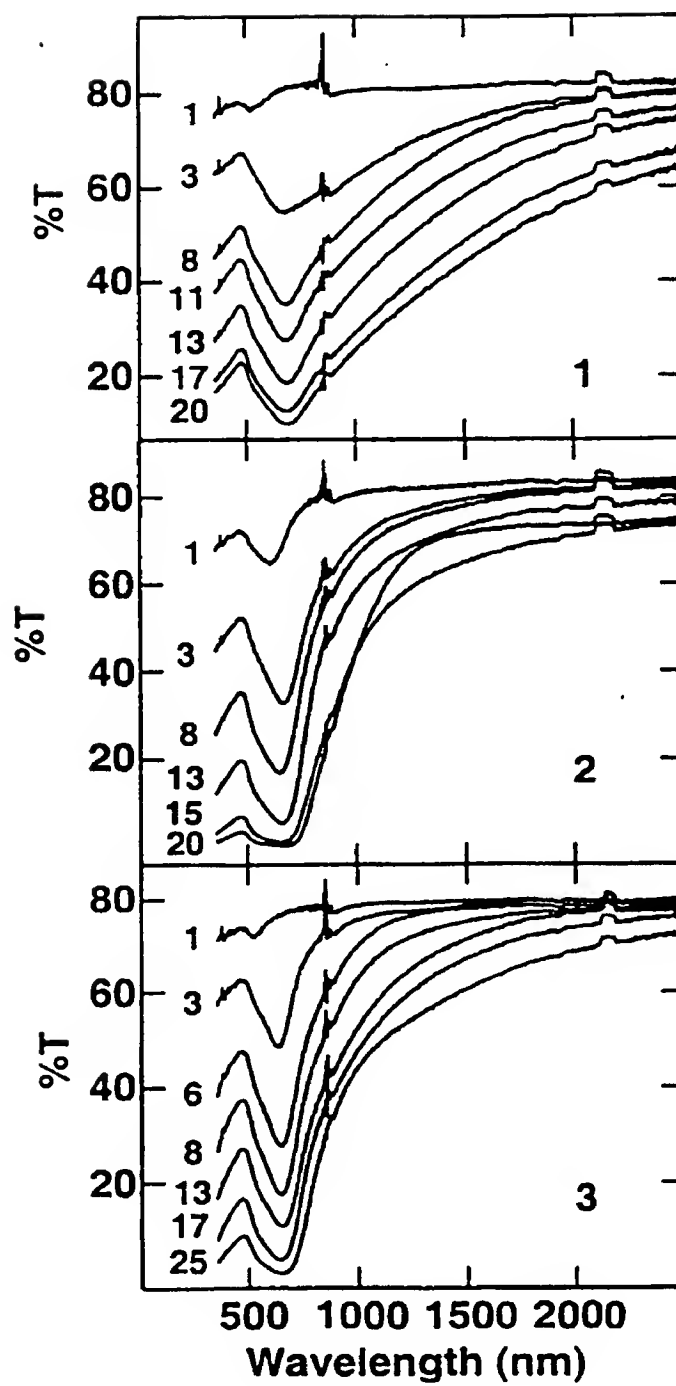


Fig. 19

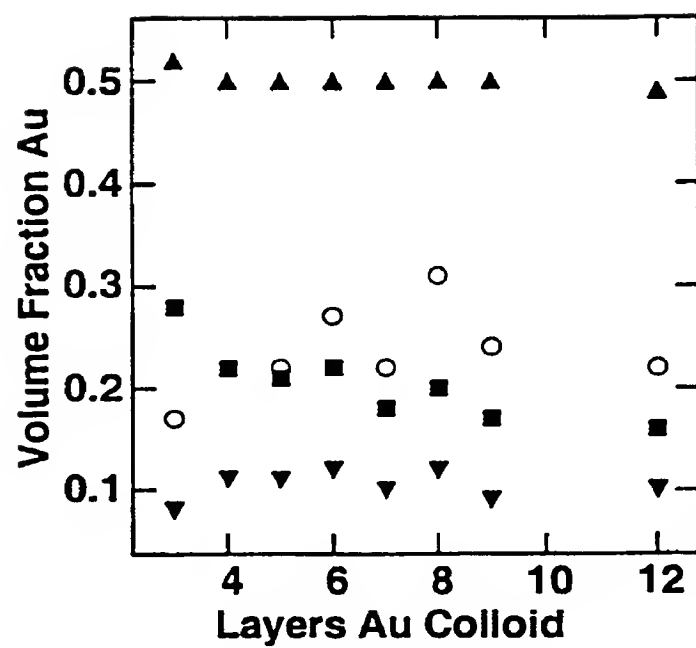


Fig. 20

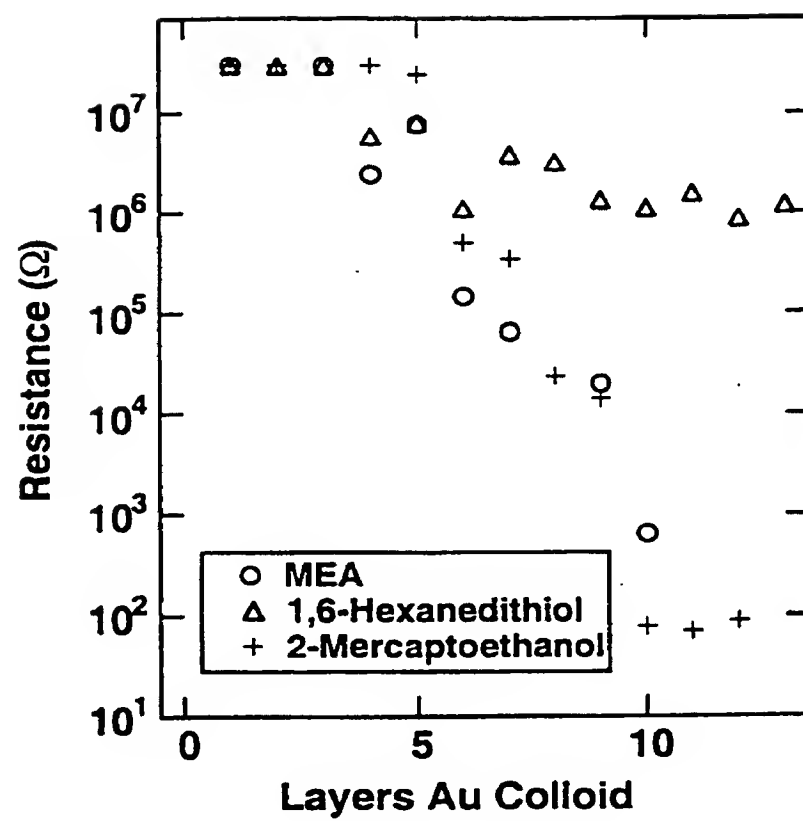


Fig. 21

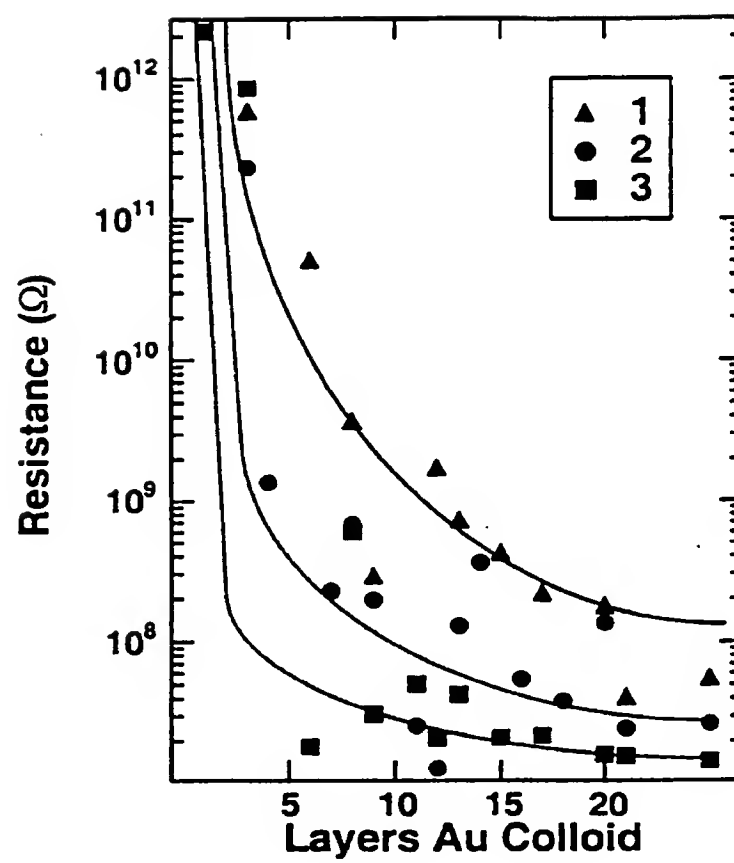


Fig. 22



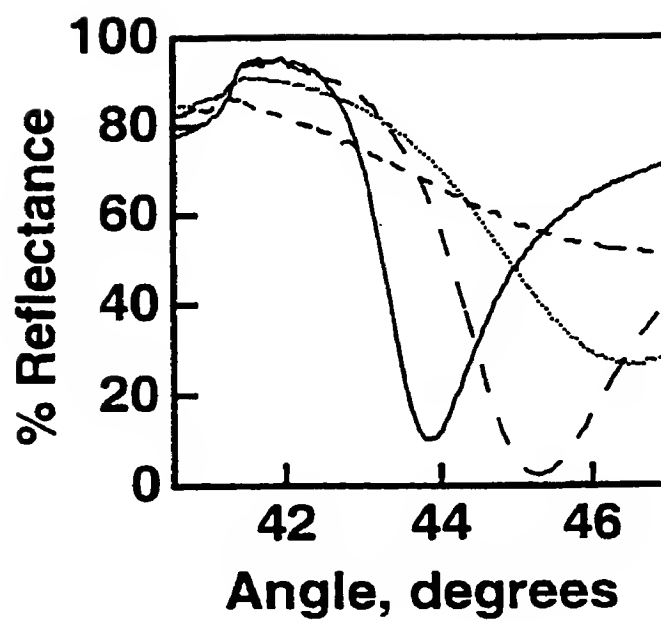


Fig. 23

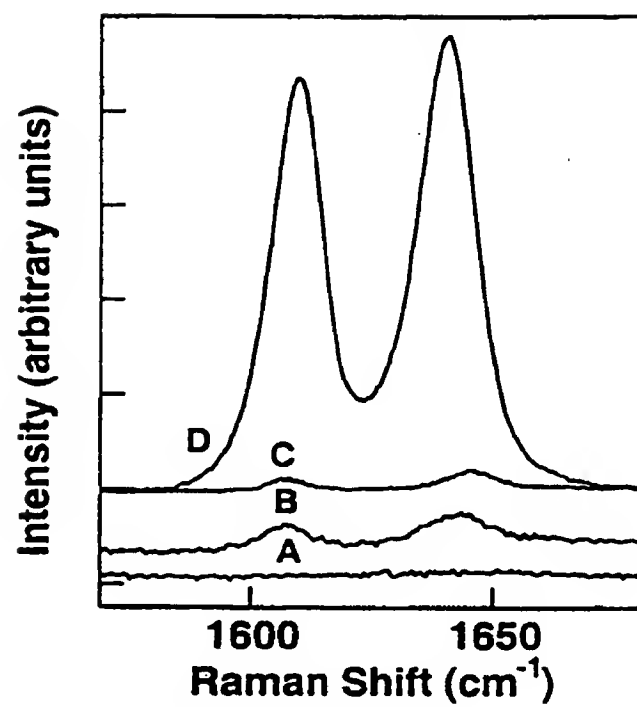


Fig. 24

## INTERNATIONAL SEARCH REPORT

International application No.  
PCT/US00/32961

**A. CLASSIFICATION OF SUBJECT MATTER**

IPC(7) :B01F 3/12; C09K 3/00

US CL :516/97; 75/721; 106/1.18

According to International Patent Classification (IPC) or to both national classification and IPC

**B. FIELDS SEARCHED**

Minimum documentation searched (classification system followed by classification symbols)

U.S. : 516/97; 75/721; 106/1.18

Documentation searched other than minimum documentation to the extent that such documents are included in the fields searched

Electronic data base consulted during the international search (name of data base and, where practicable, search terms used)

STN: colloid? (2a) (submicron? (a) particle? or nanoparticle?) and seed? (3a) colloid?

**C. DOCUMENTS CONSIDERED TO BE RELEVANT**

Category*	Citation of document, with indication, where appropriate, of the relevant passages	Relevant to claim No.
A	US 5,034,313 A (SHUMAN) 23 July 1991	1-17
A	US 5,872,013 A (LEUNISSEN et al) 16 February 1999	1-17
A	EP 0426300 B1 (SCHUTT et al) 03 June 1998	1-17

☐ Further documents are listed in the continuation of Box C. ☐ See patent family annex.

"	Special categories of cited documents:	"T"	later document published after the international filing date or priority date and not in conflict with the application but cited to understand the principle or theory underlying the invention
"A"	document defining the general state of the art which is not considered to be of particular relevance		
"E"	earlier document published on or after the international filing date	"X"	document of particular relevance; the claimed invention cannot be considered novel or cannot be considered to involve an inventive step when the document is taken alone
"L"	document which may throw doubts on priority claim(s) or which is cited to establish the publication date of another citation or other special reason (as specified)	"Y"	document of particular relevance, the claimed invention cannot be considered to involve an inventive step when the document is combined with one or more other such documents, such combination being obvious to a person skilled in the art
"O"	document referring to an oral disclosure, use, exhibition or other means		
"P"	document published prior to the international filing date but later than the priority date claimed	"&"	document member of the same patent family

Date of the actual completion of the international search 15 FEBRUARY 2001	Date of mailing of the international search report 09 APR 2001
Name and mailing address of the ISA/US Commissioner of Patents and Trademarks Box PCT Washington, D.C. 20231 Facsimile No. (703) 305-3230	Authorized officer NGOCLAN T. MAI Jean Proctor Paralegal Specialist Telephone No. (703) 308-0651

# INTERNATIONAL SEARCH REPORT

International application No.

PCT/US00/32961

## Box I Observations where certain claims were found unsearchable (Continuation of item 1 of first sheet)

This international report has not been established in respect of certain claims under Article 17(2)(a) for the following reasons:

1. ☐ Claims Nos.:  
because they relate to subject matter not required to be searched by this Authority, namely:
2. ☐ Claims Nos.:  
because they relate to parts of the international application that do not comply with the prescribed requirements to such an extent that no meaningful international search can be carried out, specifically:
3. ☐ Claims Nos.:  
because they are dependent claims and are not drafted in accordance with the second and third sentences of Rule 6.4(a).

## Box II Observations where unity of invention is lacking (Continuation of item 2 of first sheet)

This International Searching Authority found multiple inventions in this international application, as follows:

Please See Extra Sheet.

1. ☐ As all required additional search fees were timely paid by the applicant, this international search report covers all searchable claims.
2. ☐ As all searchable claims could be searched without effort justifying an additional fee, this Authority did not invite payment of any additional fee.
3. ☐ As only some of the required additional search fees were timely paid by the applicant, this international search report covers only those claims for which fees were paid, specifically claims Nos.:
4. ☒ No required additional search fees were timely paid by the applicant. Consequently, this international search report is restricted to the invention first mentioned in the claims; it is covered by claims Nos.:  
1-17

Remark on Protest

- ☐ The additional search fees were accompanied by the applicant's protest.  
☐ No protest accompanied the payment of additional search fees.

# INTERNATIONAL SEARCH REPORT

International application No.

PCT/US00/32961

## BOX II. OBSERVATIONS WHERE UNITY OF INVENTION WAS LACKING

This ISA found multiple inventions as follows:

This application contains the following inventions or groups of inventions which are not so linked as to form a single inventive concept under PCT Rule 13.1. In order for all inventions to be searched, the appropriate additional search fees must be paid.

Group I, claim(s) 1-17, drawn to method for preparing colloidal metal nanoparticles and colloidal metal nanoparticles.

Group II, claim(s) 18-25, drawn to method for preparing gold films and the gold film results therefrom.

The inventions listed as Groups I and II do not relate to a single inventive concept under PCT Rule 13.1 because, under PCT Rule 13.2, they lack the same or corresponding special technical features for the following reasons: the special technical features for group I are method for preparing colloidal metal nanoparticles and products thereof while the corresponding special technical features for group II are method for preparing gold films and products thereof.